ALMA Mater Studiorum
Universita` degli di Studi Bologna

SCUOLA DI SCIENZE

Corso di Laurea Magistrale in Astrofisica e Cosmologia

Dipartimento di Fisica e Astronomia

THE VELOCITY DISPERSION PROFILE OF THE GLOBULAR CLUSTER 47TUCANAE

Elaborato Finale

Candidato:
Sara Brizzi

Relatore:
Chiar.mo Prof.:
Francesco Rosario Ferraro

Co-relatore:
Dott. Alessio Mucciarelli
Dott.ssa Barbara Lanzoni

Sessione II
Anno Accademico 2014/2015

Contents

Abstract

Gli ammassi globulari rappresentano i laboratori ideali nei quali studiare la dinamica di sistemi ad N-corpi ed i suoi effetti sull'evoluzione stellare. Infatti, gli ammassi globulari sono gli unici sistemi astrofisici che, entro il tempo scala dell'età dell'Universo, sperimentano quasi tutti i processi di dinamica stellare noti. Questo lavoro di tesi si inserisce in un progetto a lungo termine volto a fornire una dettagliata caratterizzazione delle proprietà dinamiche degli ammassi globulari galattici. In questa ricerca, strumenti di fondamentale importanza sono il profilo di dispersione di velocità del sistema e la sua curva di rotazione. Per determinare le componenti radiali di questi profili cinematici in ammassi globulari galattici è necessario misurare la velocità lungo la linea di vista di un ampio campione di stelle membre, a differenti distanze dal centro. Seguendo un approccio multi-strumentale, è possibile campionare l'intera estensione radiale dell'ammasso utilizzando spettrografi multi-oggetto ad alta risoluzione spettrale nelle regioni intermedie/esterne, e spettrografi IFU con ottiche adattive per le regioni centrali (pochi secondi d'arco dal centro).

Questo lavoro di tesi è volto a determinare il profilo di dispersione di velocità dell'ammasso globulare 47 Tucanae, campionando un'estensione radiale compresa tra circa $20''$ e $13'$ dal centro. Per questo scopo sono state misurate le velocità radiali di circa un migliaio di stelle nella direzione di 47 Tucanae, utilizzando spettri ad alta risoluzione ottenuti con lo spettrografo multi-oggetto FLAMES montato al Very Large Telescope dell'ESO. Le velocità radiali sono state misurate utilizzando la tecnica di cross-correlazione tra gli spettri osservati e appropriati spettri teorici, e sono state ottenute accuratezze inferiori a $0.5 km/s$. Il campione così ottenuto (complementare a quello raccolto con strumenti IFU nelle regioni centrali) è fondamentale per costruire il profilo di dispersione di velocità dell'ammasso e la sua eventuale curva di rotazione. Questi dati, combinati col profilo di densità dell'ammasso precedentemente determinato, permetteranno di vincolare opportunamente modelli teorici come quelli di King (1966) o di Wilson (1975), e di arrivare così alla prima solida determinazione dei parametri strutturali e dinamici (raggi di core e di metà massa, tempo di rilassamento, parametro collisionale, etc.) e della massa totale e distribuzione di massa del sistema.

Chapter 1

Introduction

1.1 General view of globular clusters

Galactic globular clusters are extremely important astrophysical objects: they are ancient, self-gravitating stellar systems whose members of different masses are continually interacting individually and collectively. Indeed they are cosmic laboratories for testing stellar evolution and dynamics, and they are fossils of the formation epoch of our galaxy. There are several things that point out that conclusion. First the metallicity suggests that they formed in an epoch when the heavy element abundance was smaller than today; second, if the color magnitude diagrams are compared with stellar evolution models, it is found that all stars more massive than $\sim 0.8 M_\odot$ (with a main sequence lifetime of $\sim 12 Gyr$) have already turned off the main sequence. Their age provides a lower limit to the age of the Universe. While open clusters have been known to observers already, from Galileo and Herschel observations, the history of globular clusters is more recent. The first recorded discovery of an object now classificated as a globular cluster was that of NGC 6656 in 1665 by Hynes and Ihle. In 1667 Halley found the non-stellar nature of ω Centauri. As a result of increasing interest, in the eighteenth century a large number of them had been discovered. Globular clusters are found in the halo of most galaxies, in particular the most massive spirals and ellipticals, but they are observed also in a large number of dwarf galaxies. They are large and bright objects, visible over significant astronomical distances, containing $\sim 10^4 - 10^6$ stars, with symmetrical shape, orbiting around the center of the host galaxy.

There have been some attempts to link the size of the globular cluster system of an individual galaxy with the characteristics of the host galaxy itself. A parameter called 'the specific frequency', has been defined as:

$$S = N \cdot 10^{0.4(M_v + 15)} \tag{1.1}$$

and a correlation between the total number of clusters (N) and the absolute visual magnitude of the host galaxy (M_v) has been found. This suggests that interactions between galaxies might be relevant for the formation of globular clusters, and also the environment can play a role. Also the globular cluster physical properties (as the mass, the size and the shape) seem to be related to the characteristics of the host galaxy. For example it is found that the clusters which are closest to the nucleus are generally the smallest, because of the tidal effect of the galactic bulge. Most globular clusters are in elliptical orbits around their parent galaxy. In spiral systems it is likely that the orbits of some clusters actually pass through the disk and thus suffer from significant perturbations.

Since globular clusters are very old ($\sim 12 Gyr$), it follows that their stars must be in an advanced state of evolution, and the brightest stars tend to have red colors. Of course the main sequence stars make up the bulk of the mass, even though their contribution to the cluster's light output is not significant. Several magnitudes brighter than the main sequence are the stars of the horizontal branch. These contribute about 15% of the visible wavelength light of a typical globular cluster and include the RR Lyrae variables which account for about 90% of variable stars in a globular cluster. The presence of multiple stellar populations in globular clusters has been widely studied with photometric and spectroscopic studies. The presence of Na-O and Mg-Al anticorrelations suggests the formation of multiple generations of stars. The vast majority of clusters do not show any star-to-star variation in the iron peak elements, with only two major exceptions: ω Centauri and Terzan5. Hence, at a first approximation, globular clusters consist in a set of stars coeval and with the same chemical composition. Complex stellar systems, made up of different generations are modelled convolving simple stellar populations (SSPs) with an adopted star formation history. The basic ingredients of a stellar population model are the evolutionary tracks and the atmosphere models. The former trace the evolution of stars of given mass and chemical composition through the different evolutionary phases.

Globular glusters are also known to host large populations of peculiar stellar objects, like blue straggler stars, low-mass X-ray binaries and cataclysmic variables. In particular, the CMD of the globular cluster also shows a little number of stars which seem to be part of the main sequence but are above the turnoff point: they are called Blue straggler stars (BSS). They also host another type of exotica called millisecond pulsars, which are old pulsars re-accelerated.

1.2   Dynamical evolution

Beyond any mechanism of formation, the subsequent evolution of globular clusters is easier to model. The residual gas, from which the clusters form, is removed by stellar winds and radiation pressure. Moreover, when globular clusters pass through the Galactic plane, they lose interstellar gas tidally and by ram pressure. Also the peripherical stars (less bound to the cluster) contribute to mass loss, each star lost reducing the mass of the system. In the meantime the most massive stars are evolving and losing mass. Since these processes last for several billion years, it is quite probable that some clusters do not survive. When the most massive stars are already evolved, stellar dynamical effects become more important.

Gravitational interactions between individual stars orbiting around the center of the cluster tend to produce a "relaxation" in the stellar velocity distribution.

An encounter between two stars will result in a transfer of kinetic energy, depending on the ratio of the masses. If it is very high, the lighter stars may exceed the escape velociy, and "evaporation" occurs. The most massive stars lose kinetic energy and sink toward the cluster centre; over time this process causes a contraction of the nucleus, increasing the probability of encounters. In theory, the contraction of the cluster nucleus should result in a "gravothermal collapse", bringing to an infinitely dense core within a finite interval of time; however there is an increasing probability of formation of binary stars, which are able to balance the energy losses. The core collapse will halt when the center contains only a few tens of stars and interactions between them begin to produce hard binaries. It is possible that some of these binaries, the less massive ones, are ejected by interactions with the massive ones, reversing the process again and causing oscillations in the core density.

The observed density distribution of globular clusters has a central plateau and a decreasing behaviour towards the external parts and is well reproduced by the King models, see figure 1.1. By construction, these models describe equilibrium conditions driven by collisional relaxation processes. The characteristic time-scale over which a stellar system looses memory of its initial conditions because of the gravitational interactions among stars is called "two body relaxation time "and can be estimated as:

$$t_{2b} = \frac{0.1N}{logN} t_{cross} \qquad (1.2)$$

where N is the number of stars, and t_{cross} is the time needed to cross the system. The two-body relaxation time allows to discriminate collisional systems from collisionless ones, the first ones having the relaxation time much smaller than their lifetime, the latter the opposite. Globular clusters are collisional systems, the stars are individually important and their mutual interactions gradually affect the orbits of each others. In collisionless structures, stars move in a medium gravitational potential generated by all the objects present.

King models are largely used to fit the globular cluster density profiles (or surface brightness profiles) because they well reproduce the observations and, by construction, they describe a status of equilibrium with a nearly Maxwellian velocity distribution, generated by the relaxation processes.
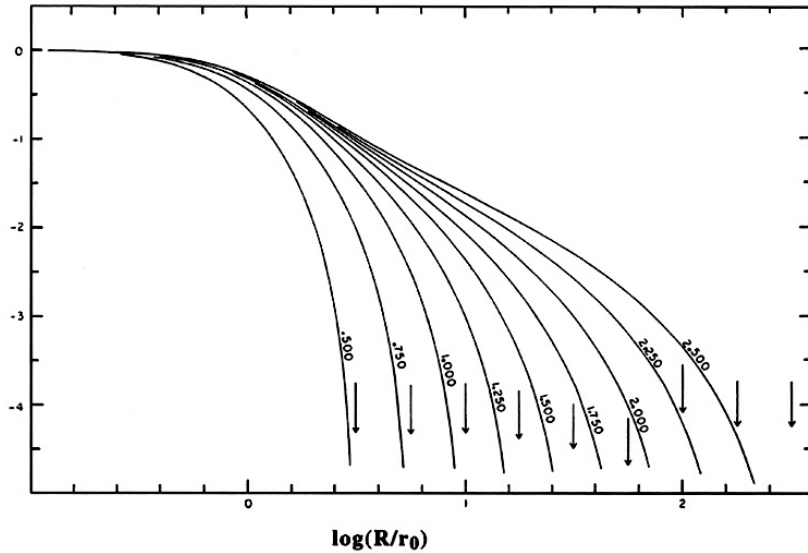

Figure 1.1: King models. The density profile is shown for values of the concentration parameter (c) ranging from 0.5 to 2.5. It can be noticed the central plateau typical of this profile.

During the collapse the central density increases and King models are not able to properly reproduce the observed profile, which develops a cusp (instead of the flat core).

Another important aspect is the possibility of the existence of an intermediate mass black hole (IMBH) at their centre: black holes with a mass ranging from $10^2 M_\odot$ to $10^5 M_\odot$. From the Magorrian relation, the best sites to form IMBHs are globular clusters. Their origin is unknown, some possibilities comprehend SN explosion from population III stars, repeated merging of stellar BHs, gas accretion on stellar BHs. They are of crucial importance for understanding the formation of galaxies and AGN since they could be the seeds of SMBHs. Moreover IMBHs may produce gravitational waves. It is known that, if they exist in the center of globular clusters, they influence the evolution and the stability of the host system. Models predict a central density cusp (not as steep as in core collapsed clusters), an intense X-Radio emission from the material accreting on it, some anomalies in the velocity or in the position of some stars and a decrease in the mass segregation. However no solid observational evidence of the existence of IMBHs in globular clusters has been obtained so far.

1.3   47Tucanae (NGC 104)

Figure 1.2: Image of 47Tuc taken from La Silla observatory with the Schmidt telescope

This work is concentrated on 47Tucanae, a Galactic globular cluster with a visual magnitude of about +4. It is the second brightest after ω Centauri and can be seen at naked-eye in the southern sky, close to the Small Magellanic Cloud.
It was discovered in 1755 by a French astronomer. Its brightness makes it an obvious target of investigation. Indeed, in 1956, Gascoigne and Burr observed a significant color gradient in the inner part of the cluster.

High resolution observations of the core made with the Faint Object Camera of the HST revealed a high density of blue stragglers. NGC 104 is also one of the nearest globular clusters, with "only" $4.6kpc$ of distance (corresponding to ~ 13400 light years), approaching us at roughly 19 km/s. Its distance from the galactic center is about $7.4kpc$ (Harris, W.E. 1996, AJ 112, 1487). The stars of 47 Tucanae are spread over a volume nearly 120 light years of diameter, covering an area of the sky of about the same apparent diameter as the full moon ($\sim 30arcmin$).

The cluster is old, well fitted by an isochrone of $13.5Gyr \pm 2Gyr$ (Archinald B.A. & Hynes S.J., Star cluster, 2010). The coordinates of the center, as determined from ACS-WFC3 and expressed in degrees, are:
$RA : 6.0237812$
$DEC : -72.0811666$
The core radius, the half-light radius and the tidal radius are, respectively, $0.44arcmin$, $2.79arcmin$, $47.25arcmin$, taken from the Harris catalog. The cluster metallicity is around [Fe/H]=-0.8 dex, (Carretta et al. 2009, Lapenna et al. 2014) and the mass is around 1.510^6 solar masses (De Rijcke et al. 2006).The present dynamical study
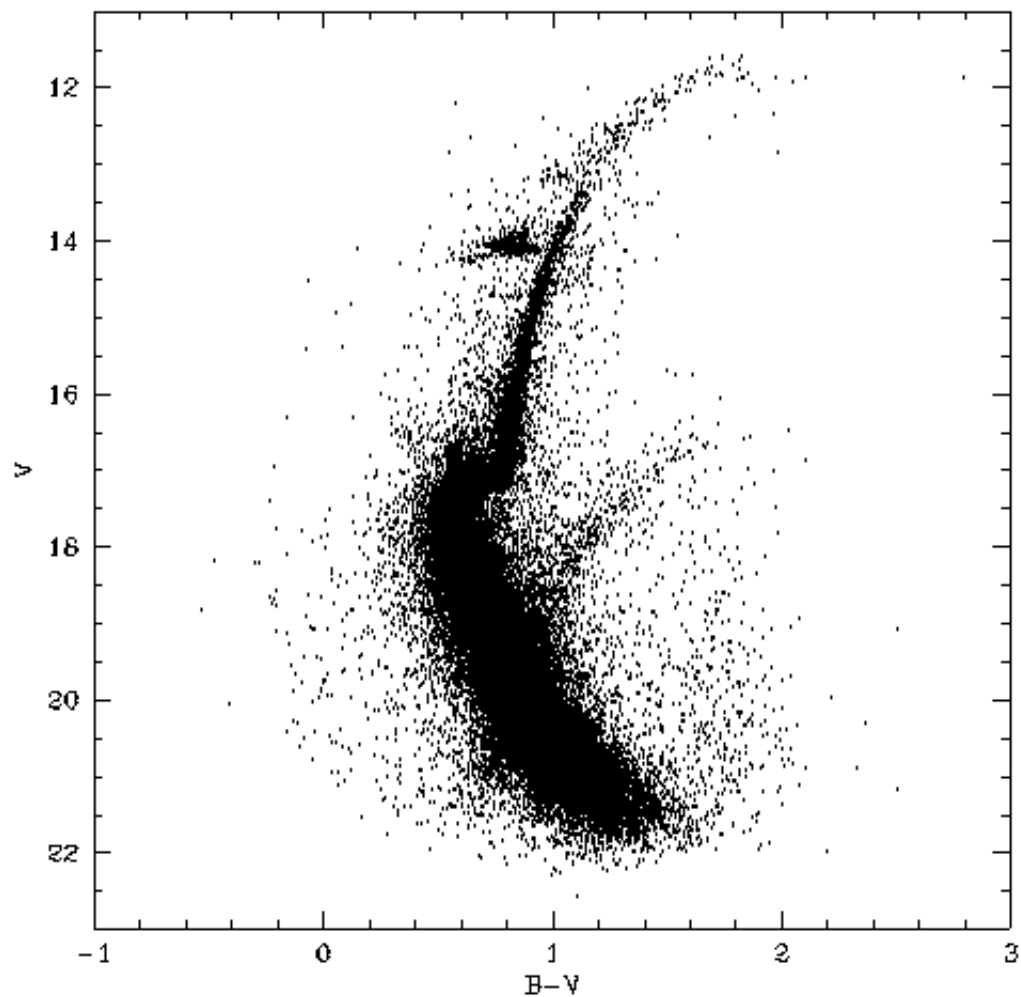
Figure 1.3: Color-magnitude diagram of the globular cluster 47Tuc. The main evolutionary sequences are well distinguishable. The "plume" at $16 < V < 19$ and $0.8 < (B - V) < 2$ is due to the stars belonging to the SMC.

is based on a combined analysis of the following kinematic profiles: (1) rotation profiles, (2) velocity dispersion profiles.

Some attempts were made to study the cluster dynamics. Since the Small Magellanic Cloud is in the background of the field of 47Tuc, with a radial velocity of $100 < V_r < 200$ km/s (Lane et al. 2011), it is clear that the samples can contain SMC stars. Lane et al. 2011 found a flattening of the velocity dispersion profile at large radii ($R \sim 35 arcmin$), probably generated by a strong external gravitational field. In addiction, they found the possibility of a two component kinematic population within the cluster. Richer et al. 2013 even proposes the exciting possibily of different stellar populations which show a significant anisotropy in proper motions. Lardo et al. 2014 and Bianchini et al. 2013 both found differential rotation in different regions of the cluster. But, at the present day, there isn't a statistically significant dataset of stars studied at high resolution, which can allow a detailed study of the dynamical properties of 47Tucanae.

Chapter 2

Data and Instrument description

2.1   VLT Multi-Object Spectrograph

The Very Large Telescope (VLT) is a telescope of the European Southern Observatory (ESO) working in the optical-infrared regime, composed by four Unit Telescopes (UTs) named Antu, Kueyen, Melipal, Yepun. Each one is equipped with a 8.2m mirror, working with alt-azimuth mount, thus allowing to point all over the sky. Each UT can work indipendently or together to form an interferometer called VLTI. The optical configuration is a Ritchey-Chrétien, each telescope has an active optics system to correct istantaneously the distortion and the atmospheric turbolence. The telescope tube itself consists of a steel structure supporting at the bottom the primary mirror (M1) in its cell, and at the top the M2 Unit by means of metallic beams called "spiders". ESO also operates four 1.8m Auxiliary Telescopes (ATs) to form a smaller interferometric array (VISA). Each telescope is protected from the external environment by a dome.
The VLT can operate in either Cassegrain, Nasmyth or Coudé focus. The stellar light is collected by the primary mirror (M1), concentrated through the combination of this and the secondary (M2) either directly to the Cassegrain focus located below the primary or to one of the two Nasmyth focii. The Coudé focus is obtained by transferring one Nasmyth focus to another location in the telescope basement by means of a relay system. From the Coudé focus the light can be sent to the combination mode focus or to the interferometric focus. When changing between Cassegrain and Nasmyth/Coudé operation, the curvature of M1 must be changed by active optics and the secondary mirror must be refocused.
The instruments mounted onto the four UTs are:

- CRIRES (*CRyogenic high-resolution InfraRed Echelle Spectrograph*) is located at the Nasmyth focus A of UT1. It provides a resolving power of up to 10^5 in the spectral range from 1 to 5.3μm when used with a 0.2 arcsec slit. It
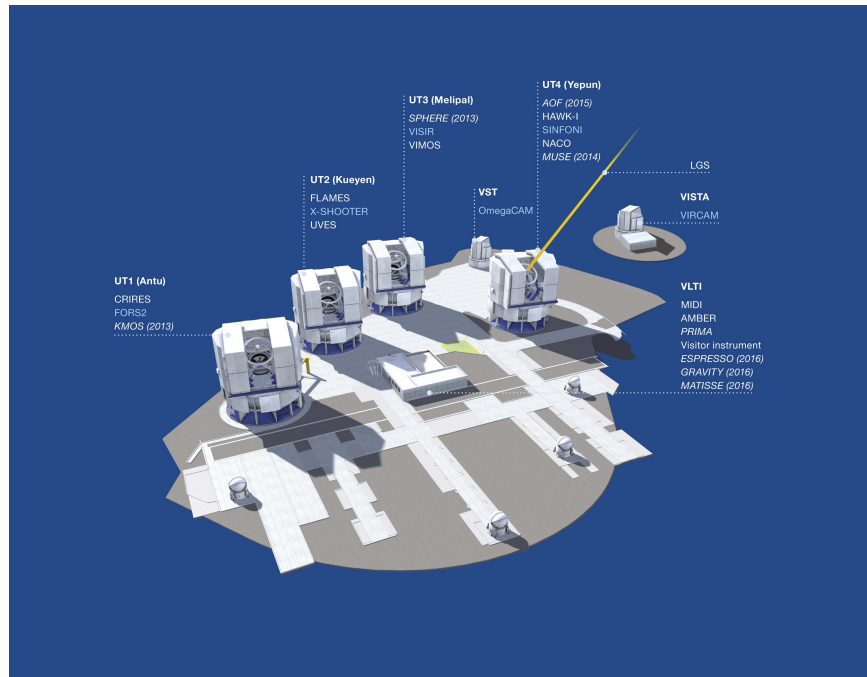
Figure 2.1: The VLT telescope

was removed from UT1 in july 2014 for an upgrade and is expected to return to Paranal in 2017.

- FORS (*FOcal Reducer and low dispersion Spectrograph*) Two versions of FORS have been built, upgraded and moved to the Cassegrain foci of different telescopes in the past years: in April 2009, FORS1 was dismounted to make room for X-Shooter, so only FORS2 is in operation. FORS2 has many modes, including multi-object spectroscopy with exchangable masks, long-slit spectroscopy (maximum spectral resolution 2600 with a 1" slit), imaging and spectro-polarimetry and high-time resolution imaging and spectroscopy. It works in the spectral range of 330-1100nm;

- KMOS (*K-band Multi Object Spectrograph*) its key feature is the ability to perform Integral Field Spectroscopy in the near-infrared bands for 24 targets simultaneously. In addition to observing multiple individual sources, KMOS has the capability for integral field mapping of contiguous areas, the spectral resolution of 3000-4000 provides velocity resolution for studies of low-mass objects and is optimal for OH-avoidance in the J & H bands. A lower resolution mode is also available in the combined H+K band;

- FLAMES (*Fibre Large Array Multi Element Spectrograph*) is the multi-object, intermediate and high resolution, spectrograph of the VLT, mounted at UT2, it can access targets over a field of view 25 arcmin in diameter. FLAMES feeds two different spectrograph covering the whole visual spectral range: GIRAFFE, which allows the observation of up to 130 targets at a time or to do integral field spectroscopy, with intermediate resolution (either 25000 or 10000) and UVES, which provides the maximum possible resolution R=47000 but can observe only up to 8 objects simultaneously;

- X-SHOOTER is a multi wavelength (300-2500nm) medium resolution spectrograph. It consists of 4 arms with the Acquisition and Guiding camera, it has 3 spectroscopic arms, each with optimized optics, dispersive elements and detectors: UVB, covering the wavelength range 300-559.5 nm, VIS, covering the wavelength range 559.5-1024 nm, NIR, covering the wavelength range 1024-2480 nm;

- UVES (*Ultraviolet and Visual Echelle Spectrograph*) is the high-resolution optical spectrograph of the VLT located at the Nasmyth B focus of UT2, designed to operate with high efficiency from the atmospheric cut-off at 300 nm to the long wavelength limit of the CCD detectors (about 1100 nm). The light beam from the telescope is split in two arms (UV to Blue and Visual to Red) within the instrument, they can be operated separately or in parallel. The maximum resolution is 80000 or 110000 in the Blue and Red Arm, respectively;

- SPHERE (*Spectro-Polarimetric High-contrast Exoplanet REsearch*) its primary science goal is imaging, low-resolution spectroscopy and polarimetry for the search and the characterization of extra-solar planetary systems at optical and near-infrared wavelengths;

- VISIR (*VLT Imager and Spectrometer for mid Infrared*) located at the Cassegrain focus of UT3. It provides diffraction-limited imaging at high sensitivity in the two mid infrared atmospheric windows: the N and Q band between 8 to 13μm and 16.5 and 24.5μm, respectively;

- VIMOS (*VIsible MultiObject Spectrograph*) is a visible (360 to 1000 nm) wide field imager and multi-object spectrograph. VIMOS operates in three different modes: Imaging (IMG), Multi-Object Spectroscopy (MOS) and with Integral Field Unit (IFU);

- HAWK-I (*High Acuity Wide field K-band Imager*) is a cryogenic wide-field imager working on the near infrared;

- SINFONI (*Spectrograph for INtegral Field Observations in the Near Infrared*) is a near-infrared integral field spectrograph fed by an adaptive optics module, the instrument can be used with a Natural Guide Star or a Laser Guide Star to provide near diffraction-limited observations. It can also be used for seeing-limited open-loop observations;

- NaCo is short for NAOS-CONICA (*Nasmyth Adaptive Optics System* and *Near-Infrared Imager and Spectrograph*) NAOS provides adaptive optics assisted imaging, imaging polarimetry, coronography and spectroscopy. CONICA is the infrared camera and spectrometer attached to NAOS, it contains several wheels carrying masks/slits, filters, polarizing elements, grisms and several cameras. CONICA was not intended to be operated without NAOS, though now observations without adaptive optics are possible.

- MUSE (*Multi-Unit Spectroscopic Explorer*) is an Integral Field Spectrograph, it has a modular structure composed of 24 identical IFU modules that together sample, in Wide Field Mode (WFM), a near-contiguous 1 squared arcmin field of view. Spectrally the instrument samples almost the full optical domain with a mean resolution of 3000.

2.2 FLAMES

FLAMES is the multi-object, intermediate and high resolution spectrograph of the VLT. Mounted at the Nasmyth A platform of UT2, it can access targets over a large field of view (25 arcmin diameter). It consists of three main components:

- A fiber positioner (OzPoz)

Figure 2.2: Backside of an OzPoz plate

The fiber positioner is able to place the fibres with an accuracy better than 0.1 arcsec during the observation. To assign the fibers to the selcted targets it is necessary to run a specific software (FPOSS) that assigns the fibres to the

selected objects. The minimum object separation is 10.5 arcsec limited by
the size of the magnetic buttons. The Fibre Positioner Observation Support
Software (FPOSS). It takes as input a file containing a list of target objects
and generates a configuration in which as many fibres as possible are allocated
to targets, allowing for the various instrumental constraints and any specified
target priorities. It produces a file containing a list of allocations of fibres
to targets, the so-called "target setup file". The OzPoz is composed of two
plates: while one plate is observing, the other one is positioning the fibres
for the subsequent observations. The dead time between two observations
is therefore limited to less than 15 minutes. OzPoz has the capability to
host up to 560 fibre per plate and four plates, but only two are used in the
FLAMES configuration. Each of these two plates feeds GIRAFFE and the
red arm of the UVES spectrographs. Plate One is hosting 132 GIRAFFE
MEDUSA buttons, 30 GIRAFFE IFU buttons (15 objects plus 15 sky), 8
UVES buttons. With Plate One it is possible to use UVES and GIRAFFE
simultaneously. In addition Plate Two contains a central GIRAFFE IFU
"Argus" facility and 15 Argus-sky buttons.

- A link to the UVES spectrograph (Red Arm) via 8 single fibres of 1 arcsec
  entrance aperture.

  UVES is a two-arm cross-dispersed echelle spectrograph covering the wave-
  length range 300 - 500 nm (Blue) and 420 - 1100 nm (Red) at UT2 of the
  VLT. It was designed to work in long slit mode but it has been possible
  to add a fiber mode fed by the FLAMES positioner to its Red Arm only.
  Each positioner plate has 8 fibres, with an aperture on the sky of 1.0 arcsec,
  resulting in a resolving power R=47000. The maximum resolution that can
  be reached with still adequate sampling, using a narrow slit, is about 80000
  in the Blue and 110000 in the Red. The two arms of UVES are equipped with
  CCD detectors, one single chip in the Blue arm and a mosaic of two chips
  in the Red arm. Only three standard UVES setups are offered, with central
  wavelenghts of 520 nm, 580 nm, and 860 nm. All 16 fibres coming from the
  two positioner plates are mounted on two parallel slits. In addition to the 8
  fibres per plate, an extra fibre is available for simultaneous calibration. For
  faint objects, one or more fibres can be devoted to record the sky contribu-
  tion. One attractive aspect is that UVES can be simultaneously used with
  GIRAFFE without the necessity for the two exposure times to be the same.

- GIRAFFE optical Spectrograph

  GIRAFFE is a medium-high resolution (R=7500-30000) spectrograph for
  the entire visible range 370-900 nm. GIRAFFE is aimed at carrying out
  intermediate and high resolution spectroscopy of galactic and extragalactic
  objects having a high spatial density. The name comes from the first design,
  where the spectrograph was standing vertically on a platform. Each object
  can be only observed in a single echelle order at once. The light comes from
  one of the 6 available slits and passes through the order sorting filter. It is
  then reflected into a double pass collimator and goes to the grating. After
  an intermediate spectrum is formed, the light is finally re-imaged on the
  CCD. The Fiber system feeding GIRAFFE consists of 2 MEDUSA slits, one
  per positioner plate, 2 IFU slits, 1 ARGUS slit, 1 Long slit for maintenance
  purposes. Special observing software (FLAMES OS) coordinates the operation
  of the different subsystems, also allowing simultaneous acquisition of UVES
  and GIRAFFE observations. Two gratings, one for high resolution mode,
  one for low-medium resolution, are mounted back to back on a turn-table.
  Filters are used to select the required spectral range, different wavelengths
  are obtained by scanning the grating along its rotation axis.
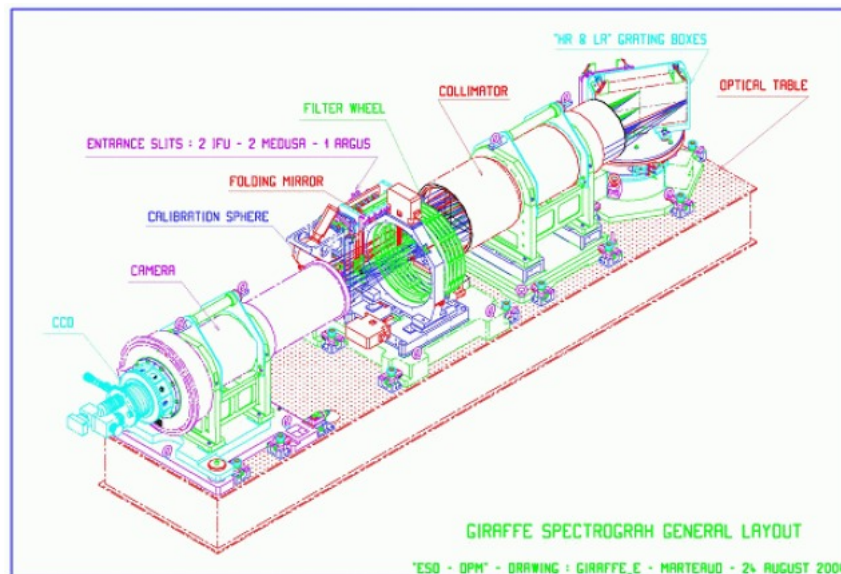
Figure 2.3: The Giraffe configuration

The fibre system includes the magnetic buttons with the coupling optics, the fibres, and the slit units. Each plate is equipped with:

- 132 MEDUSA fibres, each one has a microlens with 1.2 arcsec aperture on the sky. This mode is intended for point-like objects, which allow up to 132 separate source (including sky fibres) to be observed in one go. Two separate sets of MEDUSA fibers exists, one per positioner plate.

- 15 IFU fibres, (*Integral Field Unit*) for several applications, more extended apertures are required, while maintaining some spatial resolution and a high spectral resolving power. Each of these units is an array of 20 square microlenses,with an aperture of 0.52 arcseconds, for a total sky coverage of 2x3 arcseconds, disposed on a rectangular grid. For each plate there are 15 IFU units dedicated to objects and another 15 dedicated to sky measurements. In the latter, only the central fibre is present.

- ARGUS, a big Integral Field Unit, mounted at the centre of one plate of the fibre positioner. It consists of a rectangular array of 14 by 22 microlenses. Two magnification scales are available: "1:1" with a sampling of 0.52 arcsec/microlens and a total aperture of 11.5 x 7.3 arcsec, and "1:1.67" with 0.3 arcsec/microlens and a total aperture of6.6 x 4.2 arcsec. In addition, 15 ARGUS sky fibres can be positioned in the 25 arcmin field.

2.3   Spectroscopic Sample

We retrieved from the ESO Archive FLAMES data for stars around the GC 47Tucanae and acquired in GIRAFFE/MEDUSA mode with high resolution gratings (resolution higher than 16000). The entire sample analysed in this work consists of 4928 spectra observed within 7 different programms for a total of 666 stars:

- ID:073.D-0211(A) and 085.D-0205(A), PI:Carretta, four exposures taken in 2004 and 2010 for 140 giant stars with three different gratings: HR11, HR13, HR21;

- ID:193.D-0232(D), PI:Ferraro, 99 RGB stars with HR21 observed in 2010;

- ID:072.D-0777(A), PI:Francois, 223 stars sampled with three gratings: HR13, HR15, HR21;

- ID:188.B-3002(Q), PI:Gilmore, 110 RGB stars with HR10 and HR21;

- ID:088.B-0403(A), PI:Lucatello, 101 giant stars with HR9A;

- ID:089.D-0579(A), PI:Marino, 106 stars of the Main Sequence-Turnoff region with HR2, HR4, HR19A;

- ID:088.D-0026(A), PI:McDonald, a total of 111 giant stars in three different gratings: HR13, HR14A, HR15;

A summary of these observations can be found in Table 2.1. The observations were performed between October 2003 and September 2014, with different high resolution gratings, distributed over different spectral ranges. Because the data come from different observations each sub-sample is defined, in principle, in a different astrometric system of coordinates. In Table 2.2 are listed the principal properties of the gratings used in these programmes.

Because the data come from different observations each sub-sample is defined, in principle, in a different astrometric system of coordinates. It is therefore necessary to homogenize all the coordinates and the magnitudes to a common system. This was done with a software called "*CataXcorr*" (developed by P. Montegriffo of the Astronomical Observatory of Bologna) and devoted to cross-correlate different photometric catalogs. For each program, the catalog including the coordinates and the magnitudes of the targets has been cross-correlated with a reference photometric catalog of 47Tuc. This catalog has been obtained by combining photometric images taken with the ACS camera mounted on board the Hubble Space Telescope (for the innermost cluster region) and with the WFI camera at the 2.2 telescope of the LaSilla observatory. This reference catalog has been put into the 2MASS astrometric system.

Table 2.1: Detailed information about the sample

PI	ID	Year	N_{exp}	Grating	N_{star}
Carretta et al.	073.D-0211(A)	2004	2+1	HR11+HR13	140
	085.D-0205(A)	2010	1	HR21	112
Ferraro et al.	193.D-0232(D)	2014	1	HR21	99
Francois et al.	072.D-0777(A)	2003	2+2+2	HR15+HR13+HR21	223
Gilmore et al.	188.B-3002(Q)	2013	7	HR21+HR10	110
Lucatello et al.	088.B-0403(A)	2011	1	HR9A	101
Marino et al.	089.D-0579(A)	2012	17+13+3	HR19A+HR4+HR2	106
McDonald et al.	088.D-0026(A)	2011	3+3+3	HR13+HR14A+HR15	111

The cross-correlation among the different data-sets provided us with a total of 666 stars with repeated spectroscopic measurements, located between $20''$ and $13'$ from the cluster center. For 167 stars there are at least two independent measures, in different programmes. Most of them are RGB and AGB stars, in advanced state

of evolution and He-clump stars, see figure 2.4.
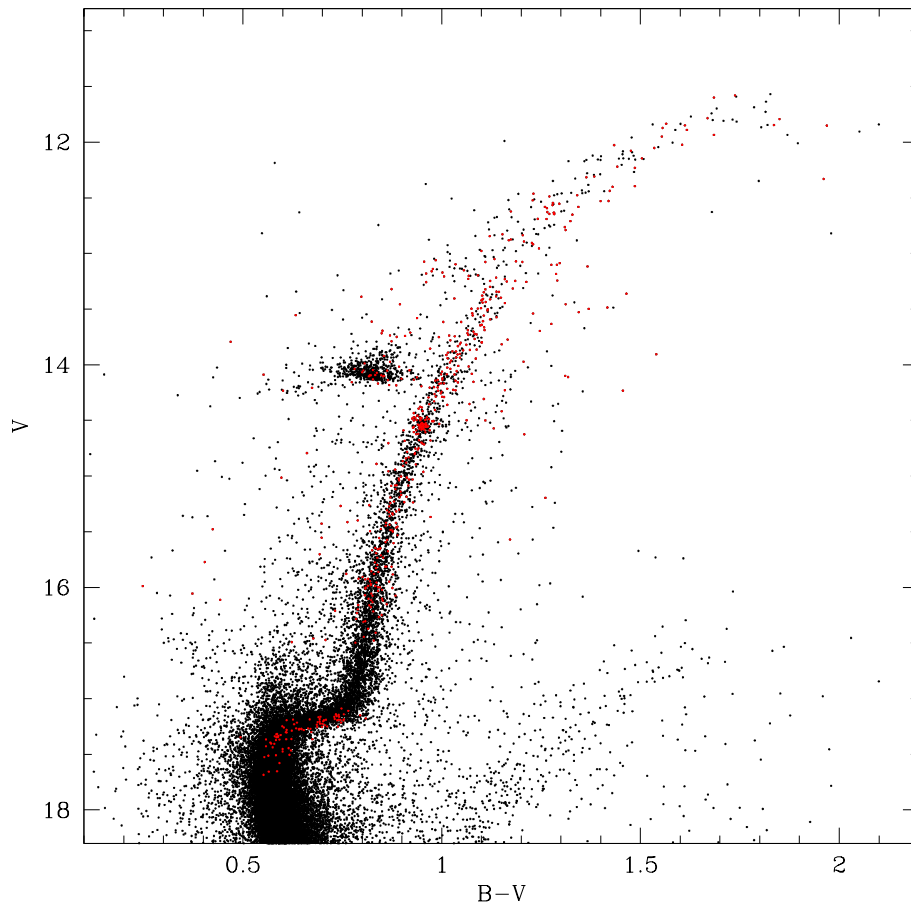
Figure 2.4: Color-magnitude diagram of the globular cluster 47Tucanae in the (V, B-V) plane. Stars marked in red are the spectroscopic targets analyzed in this thesis.

Table 2.2: Main properties (initial, central and ending wavelengths, spectral resolution) of the high resolution gratings used in this work.

ID	λ_{in} [$\dot{A}$]	λ_c [$\dot{A}$]	λ_{fin} [$\dot{A}$]	MEDUSA R
HR2	3855	3958	4050	19600
HR4	4120	4297	4392	20350
HR9A	5095	5258	5405	17750
HR10	5340	5488	5620	19800
HR11	5597	5728	5840	24200
HR13	6120	6273	6405	22500
HR14A	6308	6515	6701	17740
HR15	6607	6797	6965	19300
HR15N	6470	6650	6790	17000
HR19A	7745	8053	8335	13867
HR20A	8073	8366	8632	16036
HR21	8484	8757	9000	16200

2.4   Data Reduction

Before analyzing the data, some reduction steps need to be performed in order to obtain one-dimensional spectra:

1. Bias subtraction

2. Bad pixel correction

3. Correction of pixel-to-pixel variations of the efficiency (Flat field)

4. Fiber localization

5. Fiber tracing

6. Fiber transmission

7. Scattered light correction

8. Wavelenght calibration

All these steps are performed by using a dedicated pipeline developed by ESO (*http://www.eso.org/sci/software/pipelines/*) that provides an extracted-one-dimensional, wavelenght calibrated spectrum for each fiber.

2.4.1   The pre-reduction procedure

1. The bias is the noise of the electric devices, it represents the signal produced without input data, obtained in a short exposure with the telescope shutter closed and with light off. The masterbias, generated by the average of typically 5 bias frames, is subtracted from all the raw spectra as first step of pre-reduction. The pipeline task GIMASTERBIAS generates the masterbias and produces a bad pixel map of the detector.

2. Any detector has a certain number of pixels which work with different efficiencies and may register the information inaccurately. This happens because they are at different temperature ("hot pixels") or because they have low sensitivity ("dead pixels"). In the analysis they are fixed interpolating the signal of the close pixels.

3. Pixels have different sensitivities, some of them are more efficient in converting the light photons in electrons. Thus, the image of a uniform source of light will appear not uniform, depending on the different pixel-to-pixel variations. To correct this effect, a field uniformly illuminated (for instance

the telescope dome) is observed, in order to quantify the different sensitivity of each pixel. As for the bias an average masterflat is calculated. The task GIMASTERFLAT locates the position of the fiber, obtaining a map of the efficiency for each pixel (the "sensitivity map") on the detector.

4. As described in the previous chapter, the fibers are mounted side by side along the spectrograph slit. The direction along which the light is dispersed is called the "dispersion direction", the perpendicular one is the "cross-dispersion direction" or "spatial direction". Thus, after cleaning the detector defects, the next step of the pre-reduction process is to know where the spectrum of each fiber is positioned in the two-dimensional CCD, this is called "fiber localization". Fist, all fibers are uniformly illuminated by a calibration lamp, second the lines are cut along the dispersion direction, obtaining a set of peaks differently spaced. Each of these corresponds to a fiber. The pipeline fits each of them with a gaussian function giving for every one the center and the width. When it is found a gap and no signal is registered the fiber is declared broken.

5. Once the initial position of the fibres in known, the next step is to determine the fiber profile along the dispersion direction. Using the initial values obtained from the previous passage, the pipeline carries out a gaussian fit and new values are determined. This process is repeated until it is reached the edge od the devices.

6. Fiber are not perfect devices, the amount of lost photons depends on their energy. In a set of fibers sharing the same characteristics and having similar behaviour, some of them carry light better than others. By comparing the intensity of the extracted flat field spectra the "relative fiber transmission" can be derived. This is important for correctly doing additive operations with the fibres and for sky subtraction. For repeated targets of some gratings, multiple exposures of the same stars are avaiable. In these cases the final spectra were combined to increase the signal to noise ratio.

7. Even after the bias removal the signal may not go to zero, the remaining flux being scattered light inside the spectrograph. It has two main components: a smooth one, covering the whole CCD and proportional to the amount of light entering in the device, and a local component caused by bright objects. The latter is harder to eliminate but for an accurate sky subtraction it is necessary to remove the scattered light.

8. The dispersion axis of the spectrum is now expressed in pixels and it needs to be converted in wavelenght. This step, usually called "wavelenght calibration",

is performed by calculating a proper transformation between pixel and λ. This is done by observing, before or after the scientific observations, a reference lamp (tipically Thorium and Argon). The position, in λ, of the lamp emission lines is known, that in pixels is measured on the observed spectra. A polynomial fit of the points in the (pixel, λ) space is performed, deriving a pixel-to-λ transformation that is applied on the entire spectrum. This task is performed by the pipeline task "GIWAVECALIBRATION", producing the "dispersion solution" and the "slit geometry setup", a table including the position of each fiber on the 2-dimensional spectrum.

At the end of the pre-reduction procedure the task GISCIENCE can be executed using the products of GIMASTERBIAS, GIMASTERFLAT, GIWAVECALIBRA-TION. It does bias subtraction, flat correction, it applies the dispersion solution and finally extracts one-dimensional spectra of every fiber.

2.4.2 Sky subtraction and heliocentric correction

In order to check the accuracy and highlight possible offsets in the zero-point of the wavelength calibration, we measured the position of some sky emission lines available in the spectral range. The sky emission lines are expected to be in a rest-frame position. We compare their positions with those provided by Osterbrock et al.(1997) that lists the wavelength of the sky emission lines in the optical range. We found that the position of the sky lines well agree with the expected ones, pointing out that there is no significant offset in the wavelength calibration. This test is performed for many gratings containing spectra with evident emission lines; some exposures, *e.g.* Carretta et al. 2004, do not show them.

After this check, we need to remove from the one-dimensional spectra the contributions coming from other sources, in particular those sources of light usually referred as "sky background" and including unresolved and distant sources, the Moon reflection, Zodiacal light and ionospheric emission.

It is important to perform a good sky subtraction because the background continuum can affect the stellar continuum, making uncertainties on the abundance of the elements, while the sky emission lines can contaminate the stellar lines and the measurement of radial velocities. A case where the sky subtractions is crucial is for the spectra sampling the region of the $CaII$ triplet (e.g. the HR21 GIRAFFE/MEDUSA grating), because of the significant number of strong emission sky lines. The current version of the GIRAFFE pipeline does not perform the sky subtraction. A sky background spectrum is usually acquired observing an empty position of the field of view. In the case of the observing programs used in this work, for each FLAMES pointing typically 10-20 GIRAFFE/MEDUSA fibers have been allocated in empty sky regions. The sky spectra for a given pointing have

been combined together in order to obtain an average "mastersky" spectrum. This spectrum, including only sky continuum and lines, has been subtracted from each individual stellar spectrum of the same pointing.

Figure 2.5 shows the different phases of the procedure for the dataset taken from the program 193.D-0232(D) using HR21: the first figure shows the original spectrum before the sky subtraction, the second image is the mastersky obtained from the average of several sky spectra, the third sub-figure shows the original spectrum sky subtracted.

The spectra taken from different observatories and made at different times, must be corrected for the different position of the Earth with respect to the Sun. This step is crucial when we compare or combine together spectra of the same star acquired at different epochs. The IRAF task RVCORRECT calculates the velocity shift due to the Earth rotation and motion with respect to the Sun. This heliocentric correction is calculated by taking into account the date of observation, the position of the target and the position of the observatory. The values obtained for our sample are listed in table 2.3.
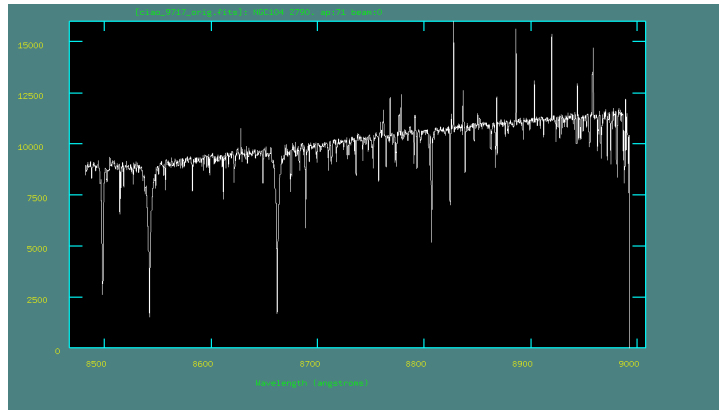
(a) *An example of an one-dimensional spectrum before the sky subtraction.*
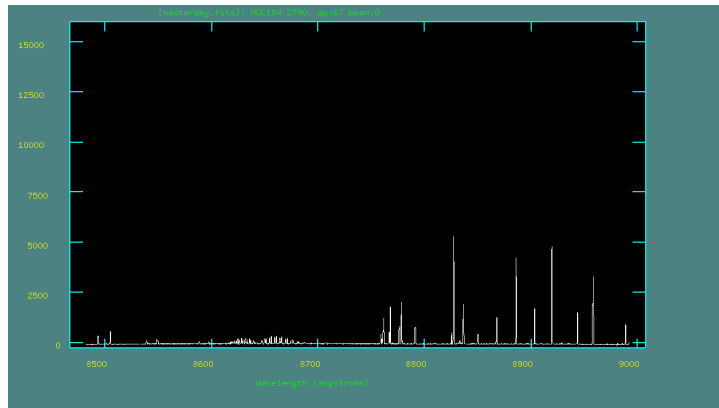
(b) *The mastersky obtained from the average of several sky spectra.*
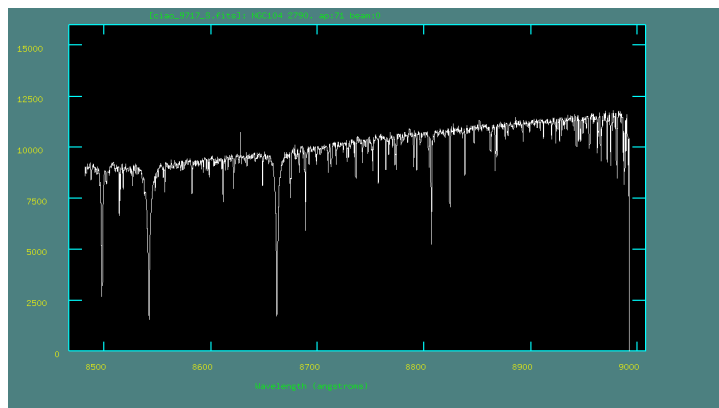
(c) *The spectrum corrected, normalized and sky subtracted*

Figure 2.5: An example of sky subtraction

Table 2.3: Values of the heliocentric correction applied to the individual observations.

Exposure	PI	Grating	Correction [km/s]
2014-09-21.02:32:21.071	Ferraro	HR21	-10.10
2013-06-29.10:05:37.516	Gilmore	HR21	10.00
2013-06-29.10:16:30.945	Gilmore	HR21	7.52
2013-07-25.10:17:54.162	Gilmore	HR21	1.91
2013-08-27.09:43:52.363	Gilmore	HR10	-5.61
2013-11-06.00:11:42.378	Gilmore	HR10	-13.86
2013-11-07.00:20:58.560	Gilmore	HR10	-13.85
2013-11-07.23:48:16.461	Gilmore	HR10	-13.84
2004-06-26.09:47:28.199	Carretta	HR11	8.06
2004-07-07.09:09:08.832	Carretta	HR11	6.99
2004-07-07.09:47:19.145	Carretta	HR13	6.99
2010-07-30.07:51:19.276	Carretta	HR21	0.92
2011-10-11.02:49:08.127	Lucatello	HR9A	-12.72
2011-11-26.00:26:40.269	McDonald	HR13	-12.90
2011-11-26.00:39:13.606	McDonald	HR13	-12.91
2011-11-26.00:51:48.394	McDonald	HR13	-12.92
2011-11-26.01:05:34.598	McDonald	HR14A	-12.92
2011-11-26.01:12:10.678	McDonald	HR14A	-12.93
2011-11-26.01:18:44.189	McDonald	HR14A	-12.93
2011-11-26.01:25:41.680	McDonald	HR15	-12.93
2011-11-26.01:31:57.619	McDonald	HR15	-12.94
2011-11-26.01:38:11.148	McDonald	HR15	-12.94
2003-10-20.23:47:21.398	Francois	HR15	-13.42
2003-10-21.00:23:20.083	Francois	HR21	-13.43
2003-10-21.00:59:46.700	Francois	HR13	-13.45
2003-10-21.01:35:08.320	Francois	HR15	-13.47
2003-10-21.02:46:18.823	Francois	HR21	-13.51
2003-10-21.03:57:39.798	Francois	HR13	-13.56

Exposure	PI	Grating	Correction [km/s]
2012-07-11.09:10:04.765	Marino	HR19A	5.05
2012-07-12.07:57:44.003	Marino	HR4	4.88
2012-07-12.08:47:50.577	Marino	HR4	4.85
2012-07-13.08:43:26.009	Marino	HR19A	4.63
2012-07-13.09:31:04.920	Marino	HR19A	4.60
2012-07-14.07:22:52.411	Marino	HR19A	4.47
2012-07-14.08:10:49.269	Marino	HR19A	4.43
2012-07-14.08:58:32.495	Marino	HR19A	4.40
2012-07-19.05:36:01.126	Marino	HR19A	3.41
2012-07-19.06:28:56.904	Marino	HR19A	3.38
2012-07-19.07:21:30.901	Marino	HR19A	3.35
2012-07-20.07:02:45.546	Marino	HR19A	3.14
2012-07-20.08:01:50.953	Marino	HR19A	3.10
2012-07-21.07:47:00.807	Marino	HR19A	2.88
2012-07-21.08:35:05.861	Marino	HR19A	2.84
2012-07-21.09:22:54.864	Marino	HR19A	2.81
2012-07-22.08:00:13.344	Marino	HR19A	2.64
2012-07-22.08:57:27.691	Marino	HR19A	2.60
2012-07-27.06:04:33.833	Marino	HR19A	1.57
2012-07-28.07:23:59.207	Marino	HR4	1.28
2012-07-28.08:32:12.989	Marino	HR4	1.24
2012-08-22.04:11:53.438	Marino	HR4	-4.35
2012-08-24.04:05:13.988	Marino	HR4	-4.79
2012-09-05.05:05:22.742	Marino	HR4	-7.35
2012-09-06.03:39:28.902	Marino	HR4	-7.50
2012-09-07.02:27:44.994	Marino	HR4	-7.65
2012-09-08.03:15:27.626	Marino	HR4	-7.88
2012-09-20.01:37:23:489	Marino	HR4	-10.00
2012-09-20.02:25:04.077	Marino	HR4	-10.02
2012-09-20.03:12:49.586	Marino	HR4	-10.05
2012-09-21.03:08:30.309	Marino	HR2	-10.21
2012-09-22.01:49:02.222	Marino	HR2	-10.32
2012-09-22.02:48:55.378	Marino	HR2	-10.36

Chapter 3

The radial velocity measures

The stellar velocity can be divided into two different components, one along the line of sight, called "radial velocity", due to the doppler shift caused by the motion of the star with respect to the observer, and one tangential component. The doppler shift can be obtained from the spectra of the stars, measuring the wavelength of absorption lines and comparing their position with the rest frame position. The doppler effect is an apparent variation of the wavelenght of a source moving along the line of sight approaching or receding from the observer: if the source is moving away (redshift) the lines are observed shifted toward redder wavelenghts, instead, if the source is approaching the observer the lines are moved toward bluer wavelenghts (blueshift). Conventionally the redshift is defined positive and the blueshift negative. The radial velocity is obtained from the equation:

$$v_{rad} = c \frac{\lambda_{obs} - \lambda_{rest}}{\lambda_{rest}} \tag{3.1}$$

where λ_{obs} is the observed wavelenght and λ_{rest} is the wavelenght of the line taken at zero redshift in a laboratory. For this work it has been used the Fourier-Cross-Correlation method implemented by Tonry & Davies (1979), within the IRAF task FXCOR. The observed spectrum is cross-correlated with a template of known radial velocity and a cross-correlation function (CCF) is computed. The CCF provides the probability of correlation between the two spectra as a function of the pixel shift applied to the observed spectrum. The CCF is then fitted with a Gaussian profile and the pixel shift corresponding to the maximum of the CCF is converted in a radial velocity. More details of this routine will be given in the Section 3.2.

3.1 Template spectra

In order to correctly measure the radial velocities it is necessary to build a suitable synthetic spectrum that will be used as template in the cross-correlation process. All the synthetic spectra used in this work have been calculated by means of the code SYNTHE. A synthetic spectrum is calculated starting from a model atmosphere, a numerical table that includes all the main properties (temperature, pressure, electron density etc.) of the atmosphere as a function of the depth. The model atmospheres used here have been calculated with the code ATLAS9: each model is defined by three main parameters, namely temperature, gravity and metallicity. For all the stars we adopted a global metallicity $[M/H] = -1.0$, the closest one to the measured cluster metallicity [Fe/H]=-0.8 dex, (see Carretta et al. 2009, Lapenna et al. 2014). In the synthetic spectrum calculation we provide also a list of all the molecular and atomic transitions that need to be included. The titanium oxyde bands are excluded because they appears only in stars with temperature cooler than $\sim$ 3700K. The spectrum is initially calculated at high resolution (R$\sim$600000) and then convoluted with a Gaussian profile in order to reproduce the instrumental profile of the corresponding GIRAFFE grating. These parameters affect the shape of the lines, see Section 3.3. For each evolutionary phase the main stellar parameters vary. In order to attribute to each group of stars reasonable average parameters (temperature and gravity) we used a theoretical isochrone extracted from the BaSTI database (Pietrinferni et al. 2004, 2006), adopting an age of 13 Gyr and a metallicity of -1.0. Four principal classes are distinguished:

- Turn off stars

- Sub Giant Branch stars

- Red Giant Branch stars

- Red Horizontal Branch and Asymptotic Giant stars (comprising the higher part of the CMD)

Although these are extended group of stars only a median value is taken, both for temperature and gravity. This is due to the fact that the radial velocity measures are not affected by the precise values of temperatures and gravities, when we use atomic transitions, characterized by symmetric profiles. The exact values of the physical properties are not needed because they affect principally the depth of the lines nor the position. The final result of the SYNTHE program is a spectrum of absorption lines for a particular evolutionary phase star, in the spectral range required. For the measures of radial velocities the synthetic spectra must be compared with the observed ones. This procedure is made with an appropriate routine

Table 3.1: Different values of temperature and gravity adopted for each group of stars to compute the synthetic spectra.

Type	log(g)	Temperature[K]
TO	3.8	5800
SGB	3	5500
RGB	2	5000
AGB/RHB	1.5	4500

of IRAF, called FXCOR.

3.2   FXCOR

FXCOR is a IRAF task aimed at deriving the radial velocity of a spectrum by using the standard cross-correlation technique as defined by Tonry & Davies(1978). This method cross-correlates a spectrum of unknown radial velocity with a template of known radial velocity. The necessary input keywords are:

- *object*, the observed spectrum for which we need to derive the radial velocity. In this work all the observed spectra provided to FXCOR are sky-subtracted and corrected for heliocentric velocity.

- *template*, the synthetic spectrum calculated with SYNTHE.

- *osample* & *rsample*, respectively the spectral region of the observed spectrum and of the template spectrum used for the cross-correlation.

The program allows to correlate only portions of spectra, if it is not necessary to take it all, but it is recommended to correlate first the whole spectral range to take an estimate of the radial velocity. The task calculates the cross-correlation function, i.e. the behaviour of the probability of correlation between the observed and template spectra as a function of the pixel shift applied to the object spectrum. The region of the CCF around the main maximum is fitted with a gaussian function, in order to derive a more precise value for the maximum of probability. Finally, the pixel shift corresponding to the maximum probability is converted in radial velocity. It is recommended for both the observed and synthetic spectrum to have a comparable resolution. Figure 3.1 shows an example of this cross-correlation. The goal is, for any good fit, to have the maximum of the cross-correlation as high

as possible: in percentage any value above 0.8 is considered excellent, but a value of 0.5 is still good. For this purpose it is important to fit a range that includes the largest number of photospheric features, avoiding spectral regions contaminated by telluric absorption lines. Figure 3.2 shows, as example, the spectrum of a RGB star observed with the GIRAFFE grating HR21, sampling the region around the Ca II triplet (the three prominent features between $8480\mathring{A}$ and $8650\mathring{A}$). Finally, the FWHM (the width of the half-height line) values are related to velocity dispersion by creation of a calibration curve, correlating the original template spectrum with itself convolved with a gaussian set of width. Figure 3.3 shows the cross-correlation function and the results of this procedure.
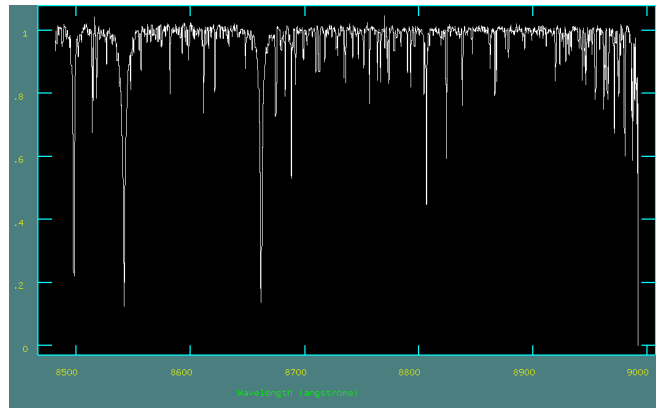
(a) *The observed spectrum.*
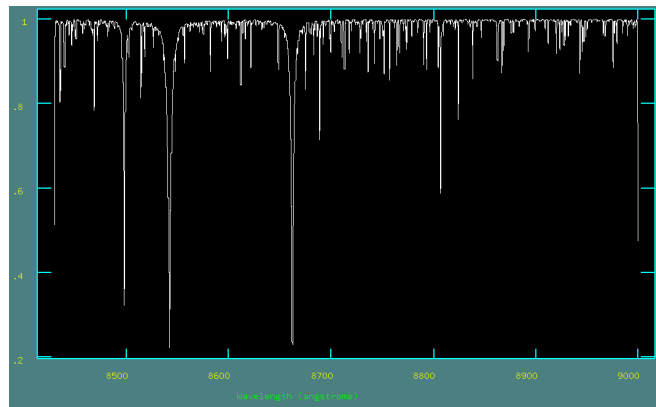
(b) *The template created with SYNTHE.*
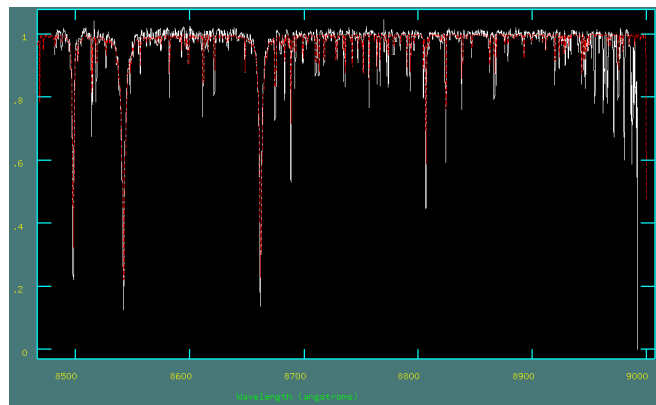
(c) *The observed spectrum corrected for its radial velocity and superimposed to the template spectrum (in red).*

Figure 3.1: An example of the FXCOR task for the star 2020142, observed with the GIRAFFE setup HR21 under the programm 193.D-0232(D).
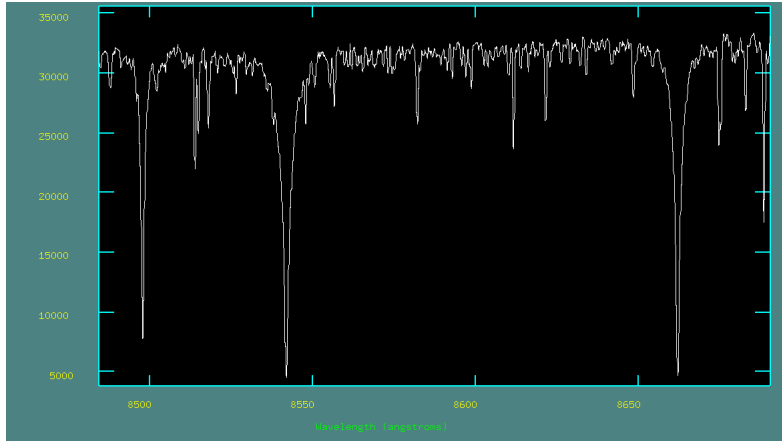
Figure 3.2: Zoom around the CaII triplet region.
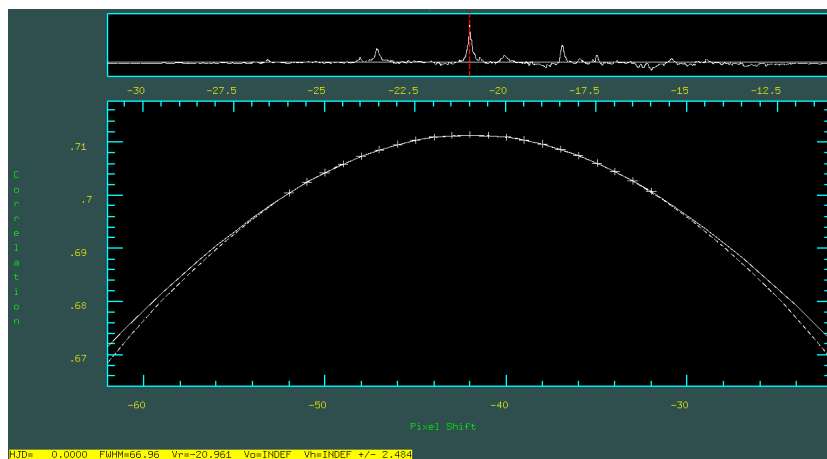
Figure 3.3: Graphic window of FXCOR showing in the upper panel the cross-correlation function, in the bottom panel there is the peak. The yellow bar reports the results of the CCF fit.

3.3 The line profile

As mentioned in the sections above, the parameters defined in the template spectrum are important for the properties of the resulting lines. The best fit of the line's profiles is a shape with a central core wavelenght, corresponding to the maximum depth, and adjacent wings, more or less widened for astrophysical effects. An useful parameter to define the intensity of the lines is the "equivalent width", in which F_c is the flux of the continuous and F_λ is the flux of the line:

$$W = \int d\lambda \frac{F_c - F_\lambda}{F_c} \qquad (3.2)$$

defined as the width, in wavelenght unit, that would have the line if it had a rectangular profile of equal area. Another parameter is the "Full Width Half Maximum" (FWHM) defined as the width of the line in the middle of the height with respect to the continuous:

$$(\Delta\lambda)_{\frac{1}{2}} = \frac{F_c - F_\lambda}{F_c - F_{\lambda_0}} \qquad (3.3)$$

where F_{λ_0} is the flux of the line corresponding to the central wavelenght.
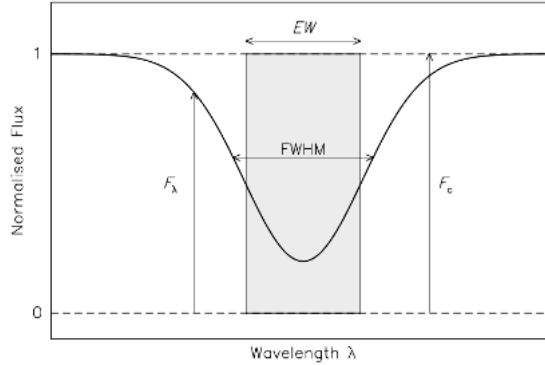
Figure 3.4: The position of W and FWHM in a line.

The final shape of a line is broadened by astrophysical effects: particle collisions, turbulence, thermal motion. The principal broadening processes are:

- Intrinsic broadening

- Collisional broadening

- Doppler broadening

- Pressure broadening

The intrinsic broadening is a consequence of Heisenberg Indetermination Principle:

$$\Delta E \Delta t \approx \hbar \tag{3.4}$$

Because of this principle the lines cannot be infinitely thin (with a shape denoted Dirac's Delta) and the photons generating them can be considered as composed by a discrete number of single, different frequencies located around the central one. The resulting FWHM is:

$$(\Delta\lambda)_{\frac{1}{2}} = \frac{\lambda^2}{\pi c \Delta t_0} \tag{3.5}$$

where Δt_0 is the interval of time necessary to obtain a level transition in the atoms. The orbitals of an atom could be perturbed by collision with other atoms or ions. Defining Δt_0 the interval between two consequential collisions, the resulting FWHM is:

$$(\Delta\lambda)_{\frac{1}{2}} = \frac{\lambda^2}{\pi c l_{mfp}} \sqrt{\frac{2KT}{m}} \tag{3.6}$$

The effect of many individual events is called "collisional broadening", if the events are more frequent is called "pressure broadening". The combined broadening of collisions and indetermination principle affects the wings of the lines, generating a damping profile.

The doppler broadening has three main origins: thermal agitation, turbulence, rotation. The rotation of a system can be easily seen with a blueshift and a redshift localized in two opposite part of the lines, the approaching part at bluer wavelenght, the one moving away at redder wavelenght. The thermal agitation broadening is generated by the atoms in constant motion in the gas. The resulting FWHM is:

$$(\Delta\lambda)_{\frac{1}{2}} = \frac{2\lambda}{c} \sqrt{\frac{2KT ln2}{m}} \tag{3.7}$$

The turbulence is particularly important for giant and supergiant stars:

$$(\Delta\lambda)_{\frac{1}{2}} = \frac{2\lambda}{c} \sqrt{ln2(v_{turb}^2 + \frac{2KT}{m})} \tag{3.8}$$

The doppler effect affects the core of the line, widens the profile and saturates the lines. When a line is completely saturated, the effect widens the wings: the resulting shape of all broadening mechanisms is called "Voigt profile". All these processes can be divided into two main broadening effects:

1. homogeneous broadening

2. non-homogeneous broadening

An homogeneous effect widens similarly every line in the spectrum, producing a Lorentzian profile. Belongs to this the finite lifetime on the excited levels of particles. Non-homogeneus effects tend to produce a gaussian profile of the lines, this category includes collisional and doppler broadening.

3.4   Sub-samples Results

We measured radial velocities for all the spectra of the 7 ESO programs described in Section 2.3. Most of the stars are in the giant evolutionary phases and the individual spectra have high signal-to-noise ratio (SNR > 40-50 per pixel). Only for the program 089.D-0579(A) (PI Marino), sampling sub-giant branch stars, the individual spectra have low SNR and they do not allow to measure the radial velocity. Hence, we combine together the individual spectra in order to enhance the SNR. For each subsample there are several values of radial velocity for the same star, because, when possible, the FXCOR analysis was splitted in two or three windows within a single spectrum. For repeated stars, finally, it was obtained a median value of these measures. The error on a measure is the value obtained from the iraf task, if only one window, comprehending the whole wavelenght range of the spectrum, is analyzed. Otherwise, for splitted spectrum analysis the error is computed as $\frac{\sigma}{\sqrt{N}}$ where N is the number of measures obtained.

Carretta dataset covers a wide spctral range, working with three different gratings: HR11 and HR13, containing a large number of spectral lines and HR21 which includes the CaII triplet (8498.02 $\dot{A}$, 8542.09 $\dot{A}$, 8662.14 $\dot{A}$) and MgI at 8806.76 $\dot{A}$. The mean value of this dataset is $< v_r > = $ -16.41 ± 0.67 km/s. This dataset is the only one, among all those analysed in this work, for which radial velocities have been published. We compare our radial velocities with those listed in Carretta et al 2009. We find an excellent agreement between the two sets of radial velocities, as shown in figure 3.5. In particular, we find an average difference of $-0.71 \pm 0.33 km/s$ and a median equal to $-0.83 km/s$.

Grating HR21 is analyzed in two other subsamples by Ferraro et al. (2010) and Francois et al. (2003). Ferraro dataset consists of 99 RGB stars, and gives an average value of radial velocity equal to $19.42 \pm 0.98 km/s$ and a median value 19.53km/s.

The sub-sample of Francois uses three different gratings: HR13, HR15, HR21, covering a large number of metallic lines. They found an average value of $< v_r >= -16.94 \pm 0.54$ km/s and a median $-17.46 km/s$.

Gilmore radial velocities are calculated with the gratings HR10 and HR21, obtaining $< v_r >= -18.04 \pm 0.87$ km/s and a median $-18.28 km/s$.

Lucatello sub-sample has only one observation made with HR9A, including

(a)

(b)
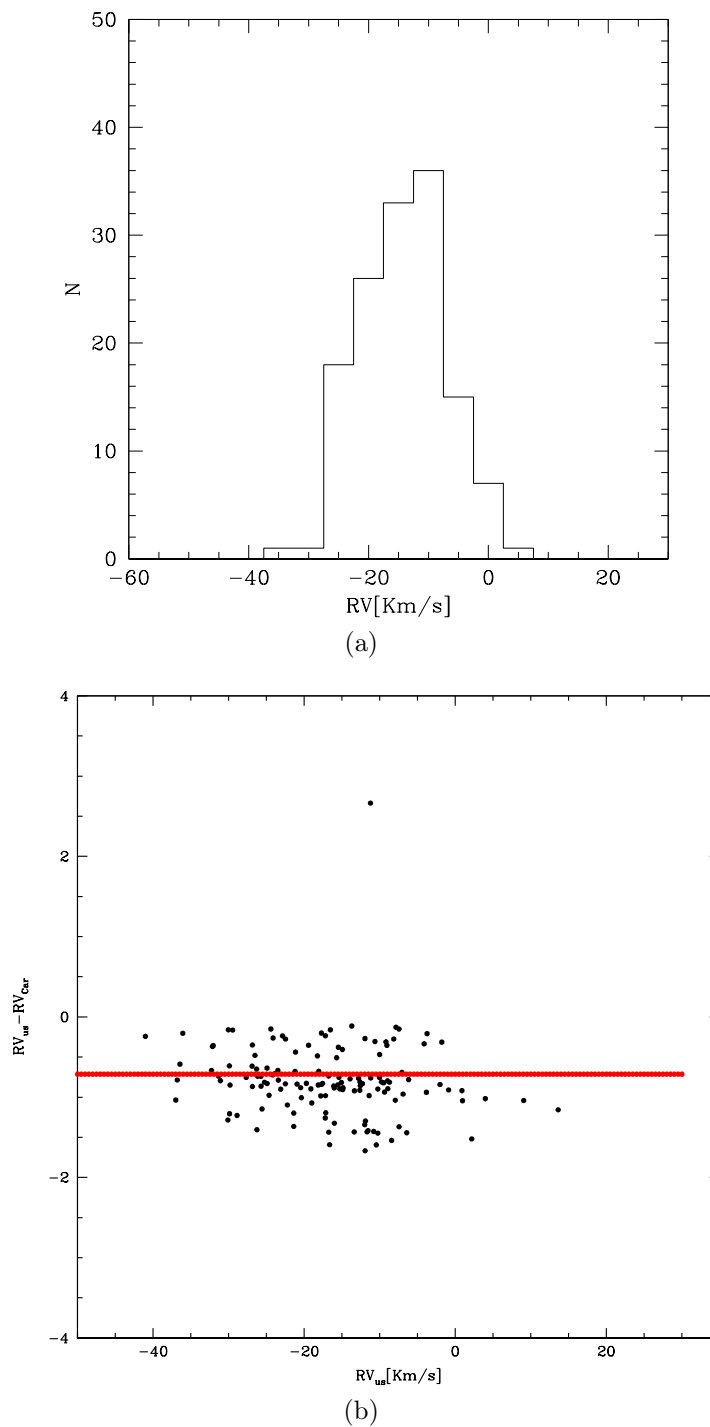
Figure 3.5: Histogram of the radial velocities obtained for the spectral sample of Carretta, in the top panel. Behaviour of the difference in radial velocities of Carretta dataset and online data against Carretta data, in the bottom panel.
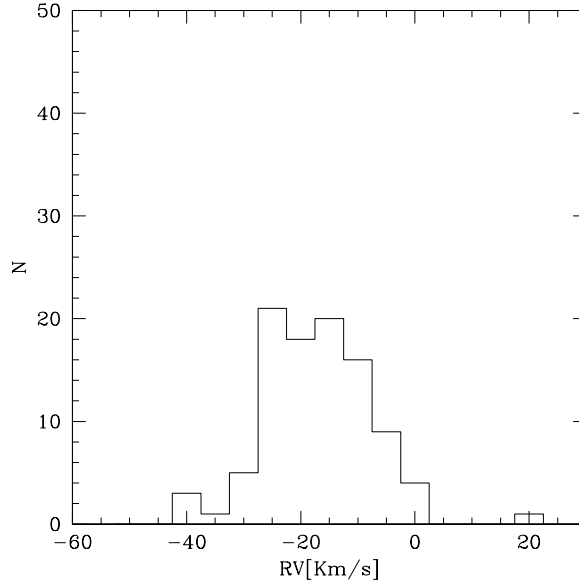
Figure 3.6: Histogram of the radial velocities obtained for the spectral sample of Ferraro

both RGB and AGB stars. The most prominent features available in the spectral range covered by the HR9A grating are the lines of the MgI triplet (5168.8 $\dot{A}$, 5174.1 $\dot{A}$, 5185.1 $\dot{A}$).

The average radial velocity of this sample is $< v_r >= -18.02 \pm 0.98$ km/s and its median is equal to -18.51km/s, see figure 3.9.

Marino sub-sample includes data of SGB and TO stars taken with three different gratings. The programmes observed with HR19A have a low signal-to-noise ratio, therefore it is produced an averaged spectrum, for all repeated stars, on which it is applied the FXCOR task to obtain a set of radial velocities with minimal confusion. HR2 contains $H\zeta$ at 3888.9 $\dot{A}$, $H\epsilon$ at 3970.1 $\dot{A}$ and the CaII doublet (3933.7 $\dot{A}$, 3968.5 $\dot{A}$). HR4 includes CaI at 4226 $\dot{A}$ and $H\gamma$ at 4340.47 $\dot{A}$. HR19 covers Na doublet (8183 $\dot{A}$, 8194 $\dot{A}$) and OI doublet (7771 $\dot{A}$, 7774 $\dot{A}$). Marino dataset gives an average value of radial velocity equal to $< v_r >= -17.39 \pm 0.70$km/s and a median value $-17.14km/s$. Figure 3.10 shows these results.

The last sub-sample is that of McDonald taken with HR13, HR14A and HR15. HR13 and HR15 include a number of metallic lines, while HR14A includes also the prominent $H\alpha$ Balmer line at $6562.95\dot{A}$. For this dataset we obtained a radial velocity $< v_r >= -17.29 \pm 0.82$ km/s and a median value $-16.88km/s$ as displayed in figure 3.11. The average radial velocities of each individual dataset are listed in table 3. We note that these values well agree each other pointing out that no significant offset does exist among the different datasets.
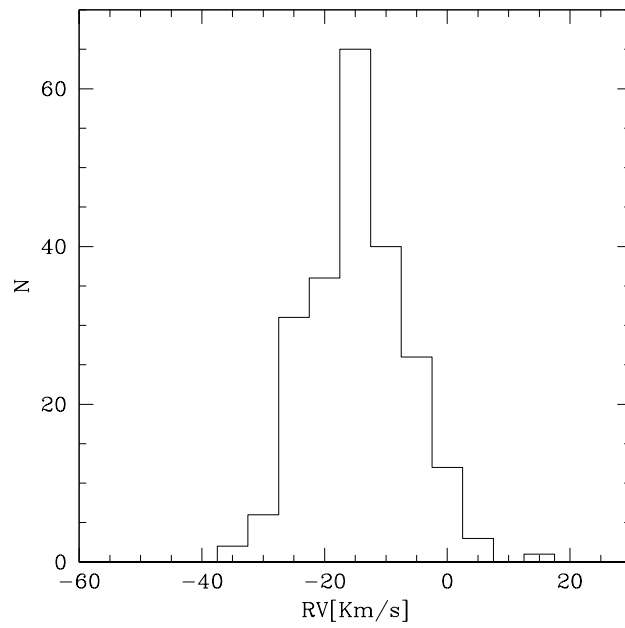
Figure 3.7: Histogram of the radial velocities obtained for the spectral sample of Francois
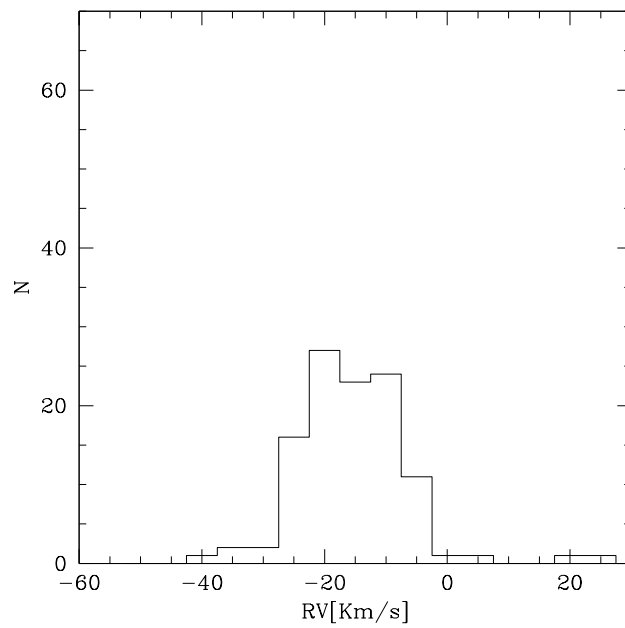
Figure 3.8: Histogram of the radial velocities obtained for the spectral sample of Gilmore dataset
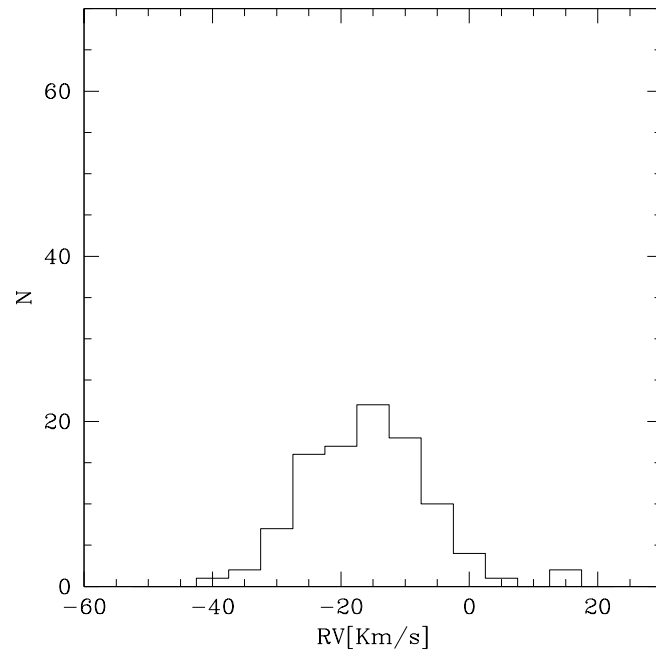
Figure 3.9: Histogram of the radial velocities obtained for the spectral sample of Lucatello.
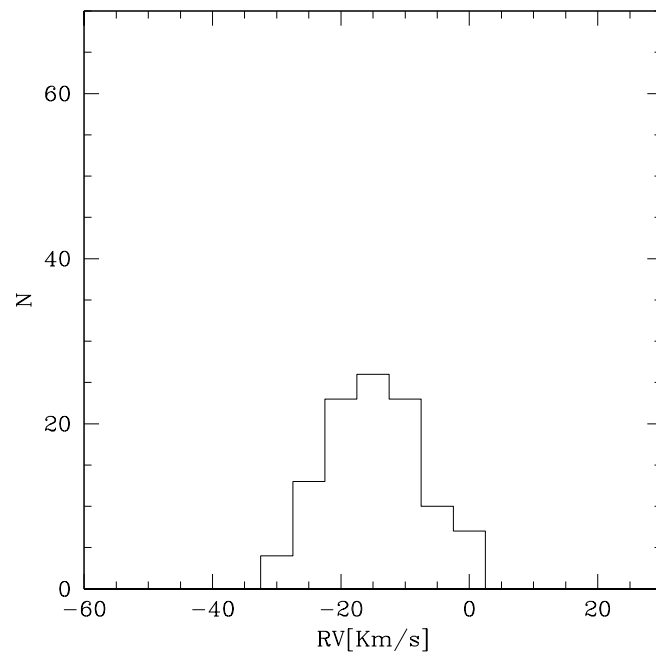
Figure 3.10: Histogram of the radial velocities obtained for the spectral sample of Marino dataset.
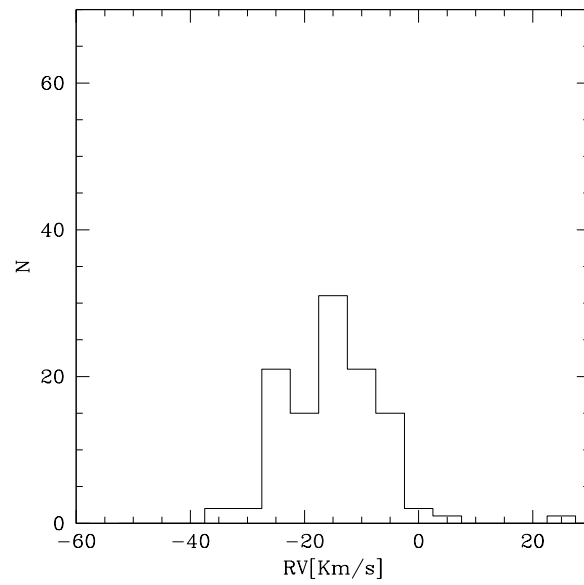
(a) *Histogram of the radial velocities obtained for the spectral sample of McDonald.*
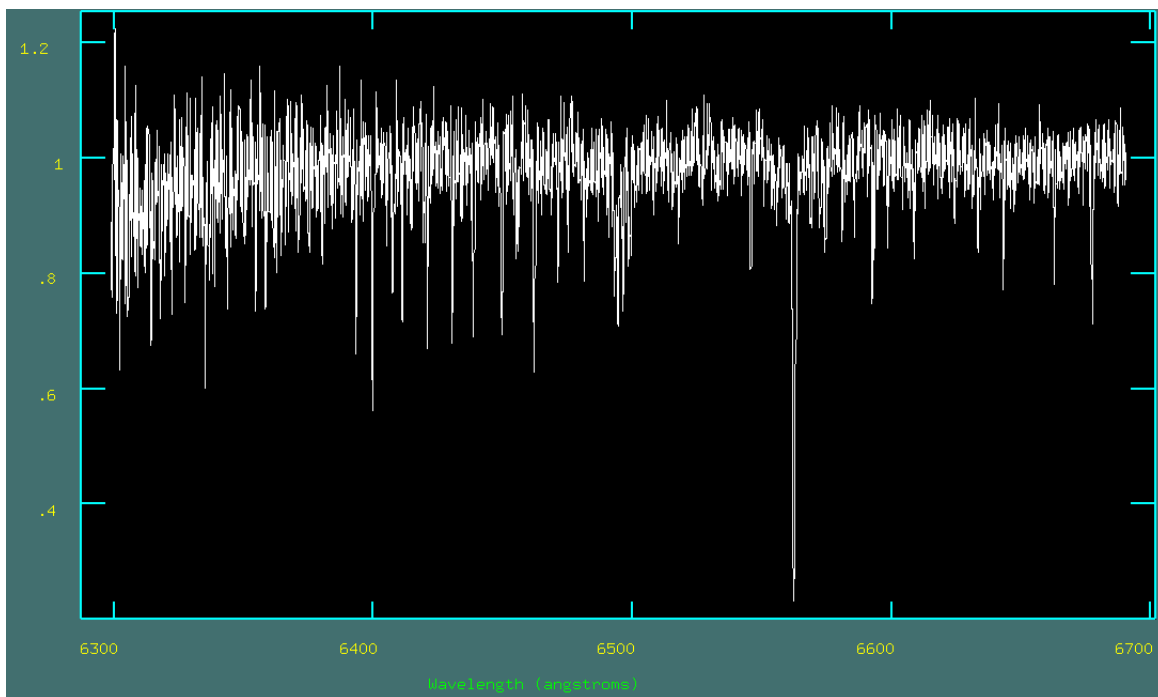
(b)   *Spectrum in HR14A grating, containing Hα Balmer line.*

Figure 3.11: Histogram of McDonald resulting radial velocities and a spectrum showing the $H\alpha$ line.

Table 3.2: Summary of the average and median radial velocity obtained for each individual dataset analyzed.

PI	Average km/s	Median km/s	σ km/s	err km/s
Carretta	-16.41	-16.46	7.92	0.67
Ferraro	-19.42	-19.43	9.75	0.98
Francois	-16.94	-17.46	8.04	0.54
Gilmore	-18.04	-18.28	9.16	0.87
Lucatello	-18.02	-18.51	9.94	0.98
Marino	-17.39	-17.14	7.20	0.70
McDonald	-17.29	-16.88	8.60	0.82

3.5 Radial velocities of 47Tucanae stars

We measured the radial velocity for a total of 666 stars in the direction of 47 Tuc. 164 of them have been observed in more than one program and thus we have independent measures of their radial velocities. For these stars, we assume as a final radial velocity the average of the different values. The associated uncertainty has been calculated as $\sigma/\sqrt{(N)}$ where N is the number of independent measures. For the stars with one only measure of radial velocity, the uncertainty is calculated as follows: for those with a large number of metallic lines in the used spectral range, the spectra has been divided in 2 or 3 sub-regions, analysed independently with FXCOR. In this case the uncertainty is $\sigma/\sqrt{(N)}$, where σ is the dispersion of the radial velocities obtained for the same spectrum and N is the number of sub-regions. Finally, for spectra where a few transitions are available (those of turnoff or subgiant stars and those with spectra sampling the region of the Halfa Balmer line) the cross-correlation has been performed by using only one spectral window. The final uncertainty is that provided by FXCOR according to Tonry & Davies (1979). The averaged values of each sub-sample are compatible, within the errors, with the value of systemic velocity listed in the Harris Catalog, equal to -17.40km/s. The final radial velocity for the whole sample of 666 stars is $< v_r >= -17.44$km/s ± 0.32km/s and a median value -17.49km/s, see figure 3.12. Figure 3.13 shows the difference of the radial velocity of each individual sample with respect to that listed by the Harris catalogue and plot radial velocities against their distance from the center of the cluster, its coordinates being :
$RA_0 = 6.0237812$
$DEC_0 = $ -72.0811666

Figure 3.14 shows the resulting histogram for the whole sample of 47Tuc radial velocities.

We compare our radial velocities with those listed by Lane et al 2011. They measured radial velocities for 4150 stars in the field around 47 tuc, within a radius of 3600arcsec from the cluster center, by using AAOmega spectra, with a resolution of 10000 on the red arm to observe the Ca triplet region, and a resolution of 3700 on the blue arm around $5200\mathring{A}$. The catalog by Lane et al. 2011 provides an average value of radial velocity $< v_r >= -16.97$km/s and a median -17.00km/s. We have in common with the catalog by Lane et al. 2011 a total of 283 stars, for which we calculated the difference of radial velocities. The comparison gives an average value, for the differences in radial velocities, equal to $+0.19 \pm 0.17$km/s and a median $+0.33$km/s, as shown in figure 3.15 and 3.16. This difference is pretty small, the dispersion is generated from the different resolutions and from different errors.
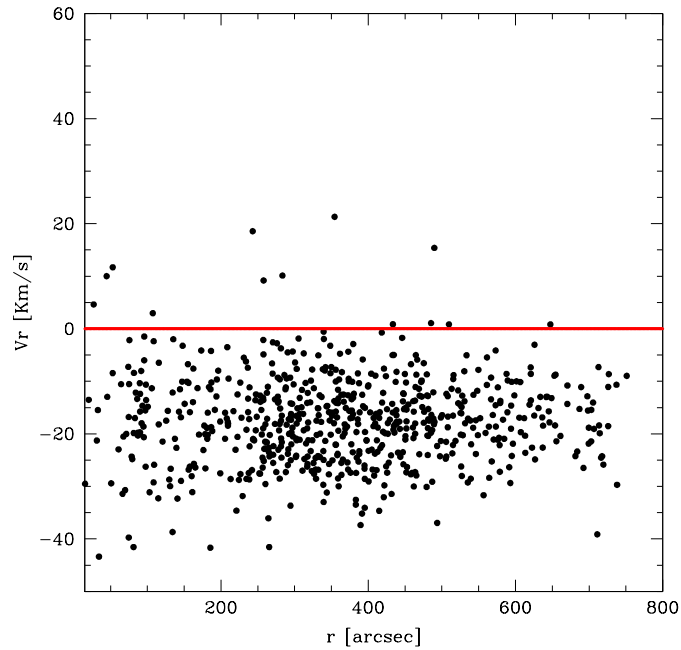
(a) *Radial velocities of 47Tucanae plotted as a function of distance from the center of the cluster. The values are concentrated around the average value of -17.44km/s.*
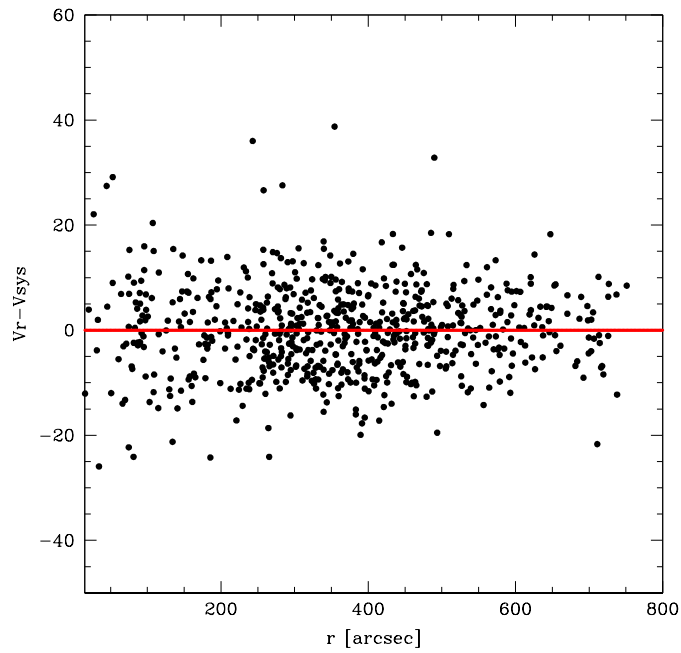
(b) *The same plot as above but centered around the zero value, because of subtraction of the systemic velocity.*

Figure 3.12: Behaviour of the radial velocities as a function of the distance from the cluster center.
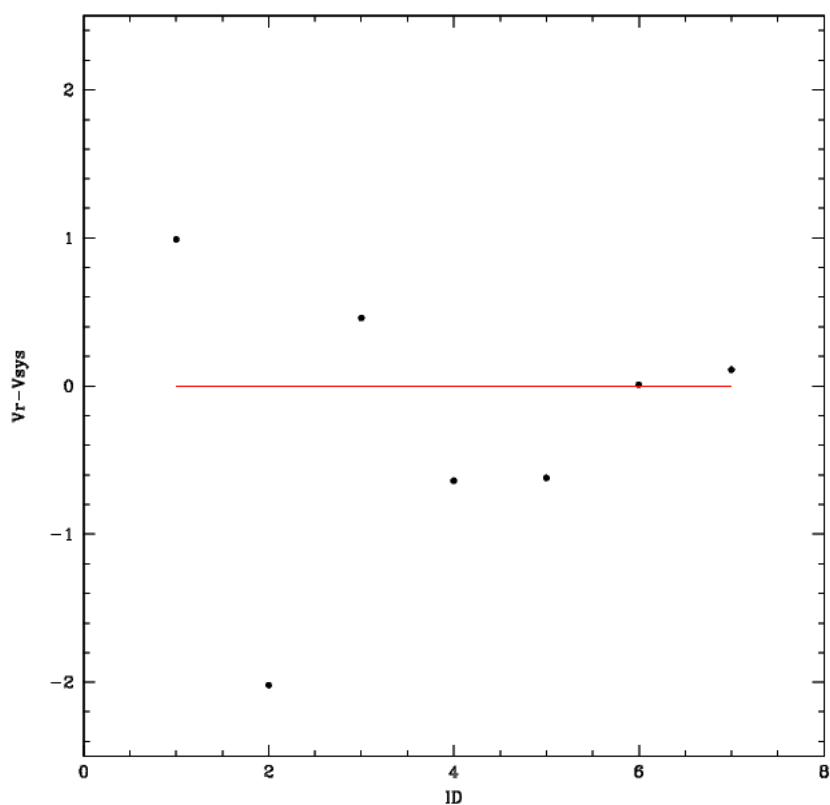
Figure 3.13: Difference between the average radial velocity of each individual sample and that listed by the Harris catalogue. On the x axis there is the identificative numbers of the programmes, taken in alphabetic order: 1 stands for Carretta, 2 for Ferraro, 3 for Francois, 4 for Gilmore, 5 for Lucatello, 6 for Marino, 7 for McDonald.
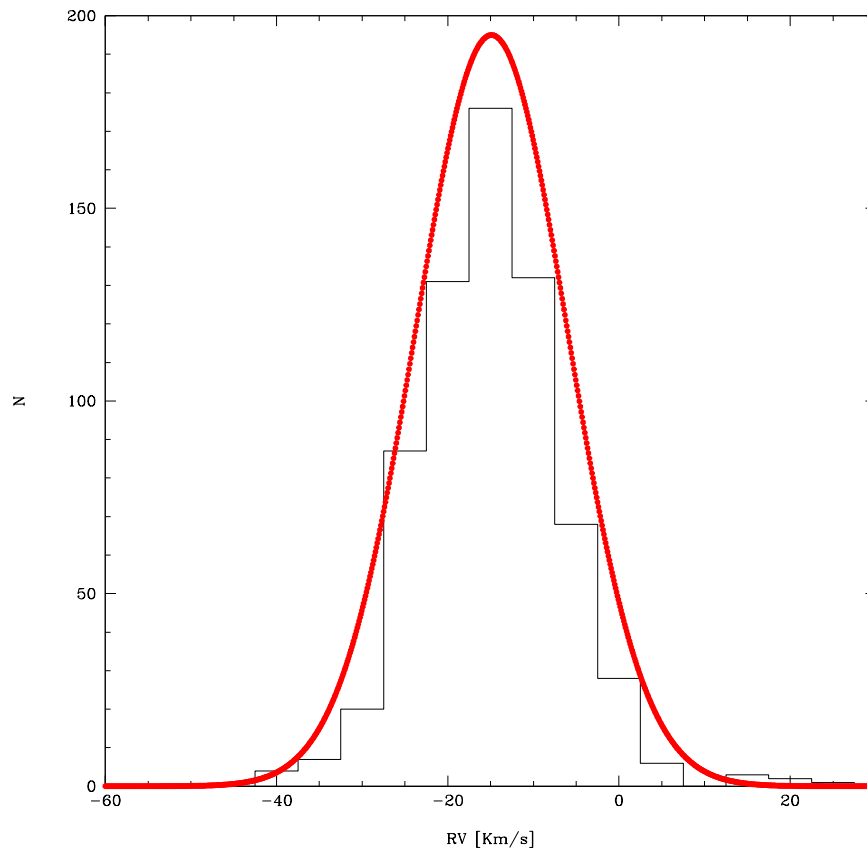
Figure 3.14: Histogram of 47Tucanae radial velocities whose peak is around -17.5km/s. The red line is a Gaussian curve with same peak and a similar dispersion.
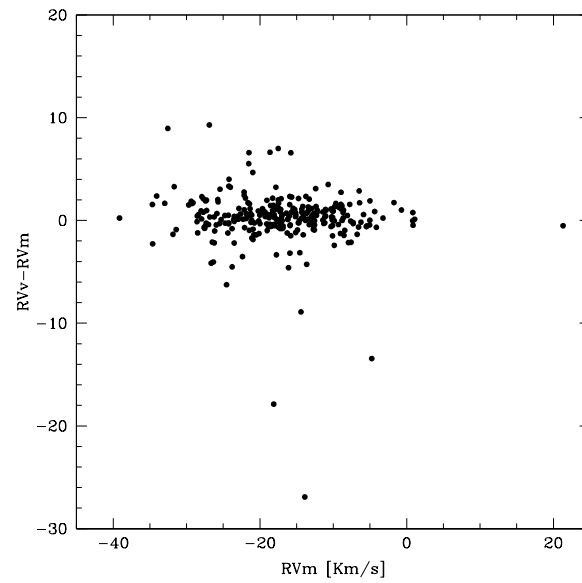
Figure 3.15: Behaviour of the difference in radial velocity for the stars in common with Lane et al. 2011 as a function of the radial velocity of our sample.
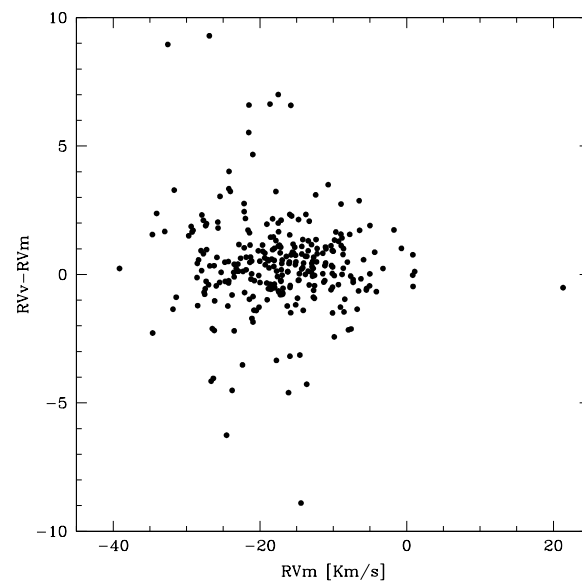
Figure 3.16: Zoom of the plot above

Chapter 4

Results

4.1 The velocity dispersion profile

In this chapter we describe the procedure to derive the velocity dispersion profile of 47 Tucanae, based on the dataset of radial velocities discussed in the previous chapters. The velocity dispersion profile shows the behaviour of the velocity dispersion as a function of the distance from the cluster center. The entire kinematic catalog is divided in radial rings and the velocity dispersion calculated in each ring by using the Maximum Likelihood Method described by Walker et al. (2006).

4.1.1 The Maximum Likelihood Principle

We start from the hypothesis that the values of radial velocities, obtained for the whole sample and indicated with v_i, have a gaussian distribution centered around the systemic velocity of the cluster (V), where $V = -17.40 km/s$ for 47Tuc. The observed dispersion of the radial velocity distribution is due to two main components: that arising from the uncertainties on the radial velocity measurements, σ_i, the other corresponding to the intrinsic velocity dispersion, σ_p. Under this assumption, the probability of having measured a given value (let's say, v_1) is:

$$P_{V,\sigma_p}(v_1) = \frac{\exp \frac{-(v_1-V)^2}{2(\sigma_1^2+\sigma_p^2)}}{\sqrt{2\pi(\sigma_1^2 + \sigma_p^2)}} \tag{4.1}$$

Then, the *Joint Probability* of the entire set of measured radial velocities is given by the product:

$$P_{V,\sigma_p}(v_1, v_2, ..., v_N) = \prod_{i=1}^{N} \frac{\exp \frac{-(v_i-V)^2}{2(\sigma_i^2+\sigma_p^2)}}{\sqrt{2\pi(\sigma_i^2 + \sigma_p^2)}} \tag{4.2}$$

For the Maximum Likelihood Principle, the cluster systemic velocity (V) and velocity dispersion (σ_P), maximize the joint probability. Therefore to obtain an estimate of these two quantities, we need to find the values $\hat{V}$ and $\hat{\sigma}_p$ that make the derivative of P equal to zero. The method consists in solving the system:

$$\begin{cases} \frac{\partial P_{V,\sigma_p}(v_1, v-2, ..., v_N)}{\partial V} = 0 \\ \frac{\partial P_{V,\sigma_p}(v_1, v_2, ..., v_N)}{\partial \sigma_p} = 0 \end{cases} \tag{4.3}$$

To simplify the calculation, we computed the derivatives of the natural logarithm of the joint probability:

$$lnP = -\frac{1}{2}\sum_{i=1}^{N} ln(\sigma_i^2 + \sigma_p^2) - \frac{1}{2}\sum_{i=1}^{N}\frac{(v_i - V)^2}{(\sigma_i^2 + \sigma_p^2)} - \frac{N}{2}ln(2\pi) \tag{4.4}$$

In fact, since the natural logarithm is a monotonically increasing function, minimizing P is equivalent to minimizing $ln(P)$. The uncertainties on these estimates can be determined taking into account that the gaussian probability distributions of $(\hat{V} - V)$ and $(\hat{\sigma}_p - \sigma_p)$ are centered around zero value and they have a joint variability described by the *Covariance Matrix*.

$$\begin{pmatrix} a & c \\ c & b \end{pmatrix} \tag{4.5}$$

$$a = \sigma_{\hat{V}}^2 \tag{4.6}$$

$$b = \sigma_{\hat{\sigma}_p}^2 \tag{4.7}$$

To determine the values of a and b values the inverse of the covariance matrix, calculated in $\hat{V}$ and $\hat{\sigma}_p$ is used:

$$A^{-1} = \begin{pmatrix} \frac{\partial^2 lnP}{\partial V^2} & \frac{\partial^2 lnP}{\partial V \partial \sigma_p} \\ \frac{\partial^2 lnP}{\partial \sigma_p \partial V} & \frac{\partial^2 lnP}{\partial \sigma_p^2} \end{pmatrix} \tag{4.8}$$

By definition of inverse matrix is obtained:

$$A^{-1} = \begin{pmatrix} \frac{b}{ab-c^2} & -\frac{c}{ab-c^2} \\ -\frac{c}{ab-c^2} & \frac{a}{ab-c^2} \end{pmatrix} \tag{4.9}$$

By equating the two matrices a system of three equation in three unknown parameters it is obtained, from which the variances can be calculated.

$$\begin{cases} \frac{b}{ab-c^2} = (\frac{\partial^2 lnP}{\partial V^2})|_{\hat{V},\hat{\sigma}_p} \\ \frac{a}{ab-c^2} = (\frac{\partial^2 lnP}{\partial \sigma_p^2})|_{\hat{V},\hat{\sigma}_p} \\ -\frac{c}{ab-c^2} = (\frac{\partial^2 lnP}{\partial \sigma_p \partial V})|_{\hat{V},\hat{\sigma}_p} \end{cases} \tag{4.10}$$

4.1.2   The velocity dispersion profile of 47Tucanae

The kinematic catalog has been divided in sub-samples corresponding to several indipendent radial bins of different size, choosen as a best compromise between spatial resolution and a statistically significant number of stars. The best selection of radial bins for the 47Tuc sample is listed in table 4.1: it consists of 5 radial bins, each containing at least 50 stars, as shown in Fig. 4.1. The radial velocities referred to the systemic velocity $V = -17.40 km/s$, taken from Harris Catalogue, are plotted as function of their radial distance from the centre.
With the current dataset we are able to measure the velocity dispersion profile between 20 arcsec and 13 arcmin.
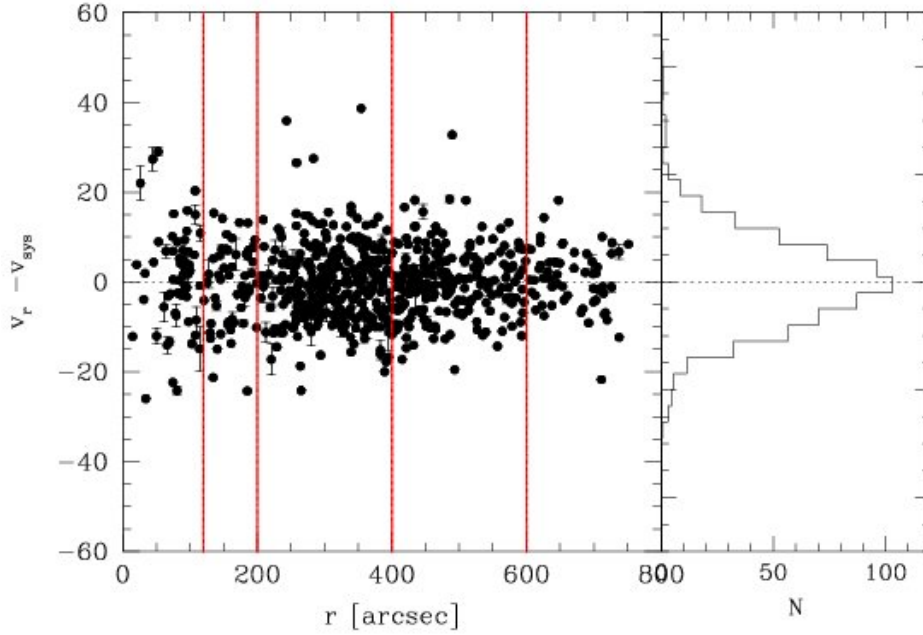
Figure 4.1: Radial velocities as a function of star distances from the center of the cluster. The vertical red lines mark the 5 radial bins selected.

Table 4.1: Internal and external radius, mean distance of the stars sampled, number of stars, velocity dispersion and its error of each bin.

$R_i[arcsec]$	$R_e[arcsec]$	$R_m[arcsec]$	N_{star}	$\sigma[km/s]$	$err_\sigma[km/s]$
14.00	120.00	78.96	45	9.80	1.03
120.00	200.00	163.90	48	8.10	0.83
200.00	400.00	312.18	254	7.50	0.34
400.00	600.00	486.54	201	6.90	0.34
600.00	800.00	665.24	52	5.90	0.60

The sample of radial velocities shown in Fig. 4.1 is obtained excluding from the sample: (a) field stars having discrepant radial velocity with respect to the bulk of the cluster stars, and (b) binary stars. Indeed, stars with velocity higher than 50km/s and errors higher than 1.5km/s are excluded. The sample contains 611 stars after this selection. On this restricted sample we applied an iterative 2.5σ-rejection in each bin, in order to include only stars with radial velocity between $v - 2.5\sigma$ and $v + 2.5\sigma$, where sigma is the velocity dispersion calculated within each bin. The final contains 600 cluster member stars. As can be seen in figure 4.1, the dispersion of radial velocities about zero decreases for increasing distance from the center. This corresponds to the progressively smaller values of σ listed in Table 4.1, ranging from a maximum of $\sigma = 9.80km/s$ to a minimum of $\sigma = 5.90km/s$, for the radial distances analyzed.

Figure 4.2 shows the standard deviation of each measure against the radial velocity. We used it to apply a first selection on error to avoid (or at least limit) the contamination from binary systems, (we excluded all radial velocities with an uncertainty larger than $1.5km/s$).

The velocity dispersion profile obtained from these data is shown in Fig. 4.3 together with its best fit King model. This is obtained for $r_c = 28arcsec$ and $\sigma_0 = 11.6km/s$, in good agreement with the value determined by Gebhardt&Fischer (1995) who found $\sigma_0 = 12km/s$. As expected (since no radial velocities are measured within the innermost 13 arcsec), this profile gives no information about the presence of an IMBH in its center. Indeedthe observations are made beyond the King model's plateau, bringing no evidence of a central cusp.

Figure 4.4 provides a comparison between our dataset of stellar radial velocities and the catalog by Lane et al. (2011). They derived radial velocities with observations made by AAOmega instrument of Anglo-Australian Telescope (AAT) using different gratings, extending in a radial interval from 11arcsec to 3630arcsec, including field stars with radial velocities spanning the range $[-1814.3, 1010.5]km/s$. These authors hypothesize that the flattening of the dispersion profile on the exter-
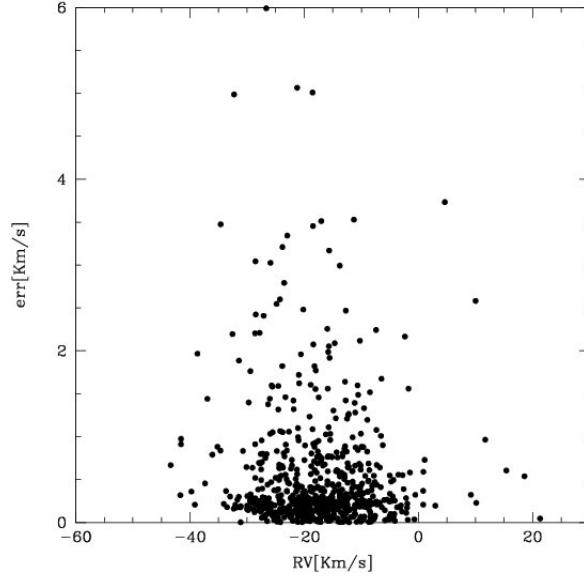
Figure 4.2: Plot of standard deviation against radial velocities. It is used to identify possible binary systems.

nal radii could be generated by a strong external gravitational field, which affects stars more than the cluster gravity, without requiring the presence of dark matter or a modified gravitational theory. Other possibilities involve the evaporation of low-mass stars due to two-body interactions, past merger, two kinematically distinct populations of stars. In subsequent works they discuss the possibility of a two-component kinematic population within 47Tucanae, which could have formed from two individual clumps in the protogalactic cloud (Lane et al., 2012). The values obtained for our dispersion profile are comparable, within the errors, with those determined by Lane et al., 2011, with the central point being the most discrepant.

4.1.3   Checks on the velocity dispersion profile

We discuss the impact on the velocity dispersion profile of different assumptions for the radial binning. Figure 4.5 shows the velocity dispersion profile obtained with a different binning, chosen thus to have approximately the same number of stars, in every radial annulus. The associated values are written in table 4.2.
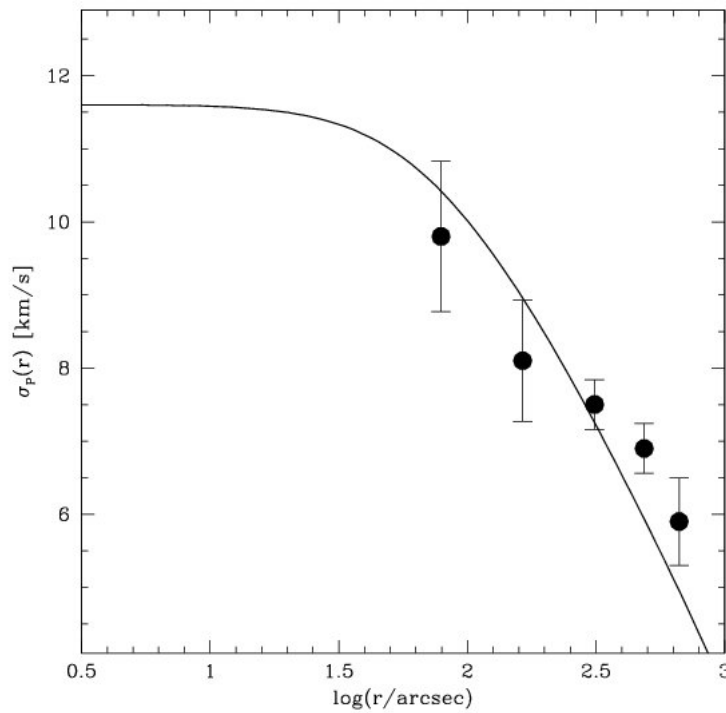
Figure 4.3: The velocity dispersion profile of 47Tucanae obtained by dividing the entire dataset in the 5 radial bins listed in Table 4.1. Superimposed to the velocity dispersion profile is the best-fit King model, calculated with σ_0=11.6km/s and r_c=28arcsec.
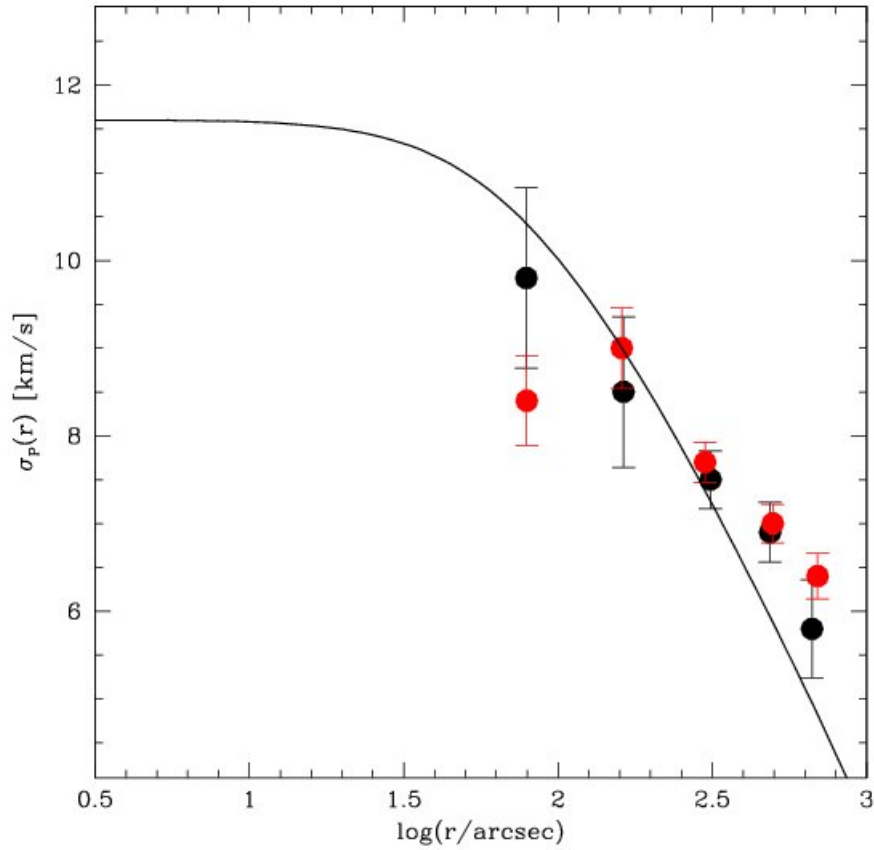
Figure 4.4: Velocity dispersion profile obtained with our dataset (black points) in comparison with that obtained by Lane et al.(2011, red points). The results are comparable within the error. The largest discrepancy is found for the innermost data point and is due to the different rejection criterion adopted.
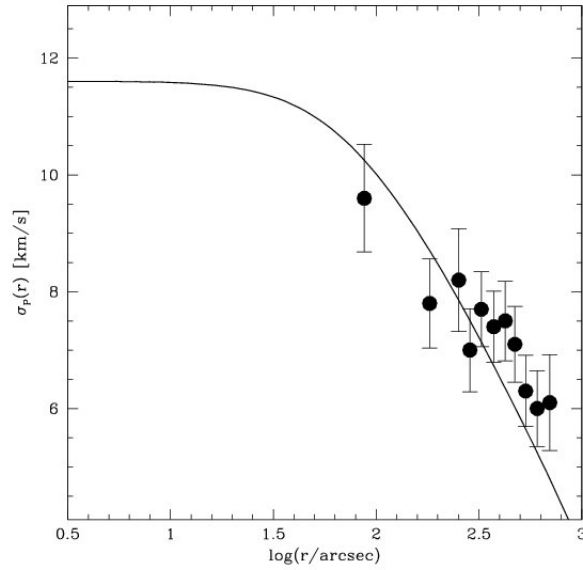
Figure 4.5: Velocity dispersion profile obtained with a different choice of the radial binning. Here each bin contains approximately the same number of stars (N∼50).

Table 4.2: Internal and external radius, mean distance of the stars sampled, number of stars, velocity dispersion and its error in each radial bin (defined in order to have a similar number of stars).

$R_i[arcsec]$	$R_e[arcsec]$	$R_m[arcsec]$	N_{star}	$\sigma[km/s]$	$err_\sigma[km/s]$
14.00	140.00	87.58	54	9.60	0.92
140.00	230.00	182.11	52	7.80	0.76
230.00	270.00	252.08	47	8.20	0.88
270.00	300.00	285.72	49	7.00	0.71
300.00	350.00	324.59	71	7.70	0.64
350.00	400.00	373.21	75	7.40	0.61
400.00	450.00	424.49	63	7.50	0.68
450.00	500.00	472.49	62	7.10	0.65
500.00	570.00	533.43	53	6.30	0.61
570.00	650.00	606.88	47	6.00	0.65
650.00	800.00	698.12	28	6.10	0.82

In fig. 4.5 each bin contains approximately 50 stars, but the resulting profile is over-sampled in the external part. Some of these points can be included in larger bins, not taking into account the number of stars, and the resulting profile, shown in fig. 4.6 is less crowded. It is similar to the best profile shown above. The values corresponding to the data points shown in Fig. 4.5 are listed in Table 4.3.
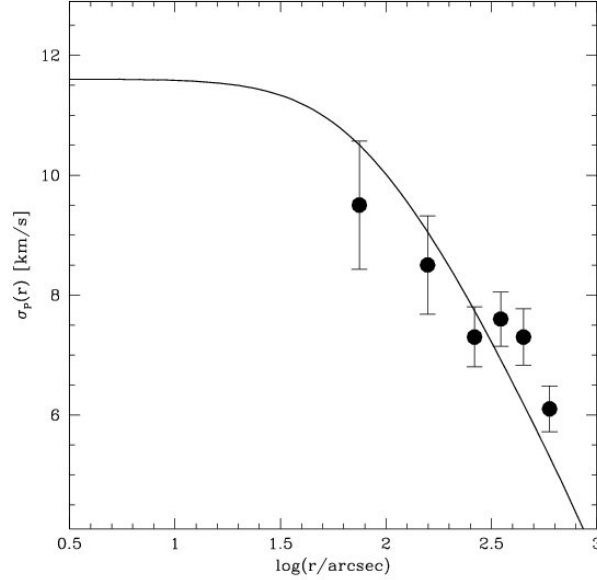
Figure 4.6: Another example of how a different choice of the radial binning affects the resulting velocity dispersion profile.

Table 4.3: As in Tables 4.1 and 4.3, but for a different choice of the radial binning.

$R_i[arcsec]$	$R_e[arcsec]$	$R_m[arcsec]$	N_{star}	$\sigma[km/s]$	$err_\sigma[km/s]$
14.00	100.00	74.80	39	9.50	1.07
100.00	200.00	157.66	54	8.50	0.82
200.00	300.00	262.89	108	7.30	0.50
300.00	400.00	349.73	146	7.60	0.45
400.00	500.00	448.49	125	7.30	0.47
500.00	800.00	596.80	128	6.10	0.38

4.2   Cluster rotation

Globular clusters have long been considered simple quasi-relaxed non rotating stellar systems, characterized by spherical symmetry and velocity isotropy. Instead, more recent studies have shown that internal rotation can be non negligible in some GCs, and its effect, with external tides and pressure anisotropy, could be responsible for the flattening and the morphology of the systems. Several globular clusters show an internal rotation of $(2-4)km/s$, (Bellazzini et al.2012, Lardo et al.2014, Bianchini et al. 2013). We therefore used our dataset to investigate the presence of systemic rotation in 47 Tucanae.

To this aim, following Van de Ven et al. (2006), we computed the position (X,Y) of each star in the plane of the sky, with respect to the cluster centre:

$$X = -r_0 cos\delta sin(\alpha - \alpha_0) \tag{4.11}$$

$$Y = r_0[sin\delta cos\delta_0 - cos\delta sin\delta_0 cos(\alpha - \alpha_0)] \tag{4.12}$$

where r_0 is the conversion factor from degree to arcseconds, and (α, δ) and (α_0, δ_0) are the right ascension and the declination (in degree) of the star and of the cluster center, respectively. The first step is the identification of the position angle (PA) of the rotation axis, with respect to the line of sight, in the plane of the sky. The PA is the angle between the rotation axis and the north direction, measured from east to north. The sample of measured radial velocities is divided into two halves by an axis, with a given PA and passing through the centre of the cluster, and for each of the two halves we computed the mean $< v_r >$. The PA is varied in steps of 10 degrees and the difference between the mean velocities obtained on the two halves is plotted against PA. The resulting pattern is fitted with a sine function:

$$F = Asin(x + \phi) \tag{4.13}$$

where $\phi = 270° - PA$, the amplitude (A) gives an estimate of the rotation velocity value and x is an angle which can assume every value contained between 0 and 360 degrees. The PA corresponding to the maximum difference in velocity is assumed as the position angle of rotation axis and is labelled as PA_0. A χ^2 test is performed to determine the best-fit values of A and PA, and the results are used to rotate the Cartesian coordinate system in the plane of the sky aligning Y' direction along the axis and and the X' direction along the axis perpendicular to Y'.
A diagram plotting the measured stellar velocities (referred to the cluster systemic velocity) as a function of the distance (X') from the rotation axis projected along the direction perpendicular to it shows the rotation curve: the sample is divided in four sub-samples with $x < 0$ and $x > 0$ and approaching or receding velocities. Two cases can be distinguished:

1. No rotation is found if the star distribution is homogeneus in the four subpanels and the velocity is rather symmetric with respect to the axes;

2. There is rotation if the stars are mainly distributed in two diagonally facing sectors.

A *Kolmogorov-Smirnov* (KS) test is then performed in order to check whether the two distributions are extracted from the same parent population. If the probability is almost null, the cluster has a non negligible rotation.

4.2.1   The rotation curve

We applied this procedure to the data set of radial velocities measured in 47 Tucanae. The upper plot of Fig. 4.7 shows the difference between the mean radial velocities determined in the two halves of the sample, as a function of the position angle PA. This is obtained by considering the enrtire data set analyzed, and the continuous curve presents the best-fit sinusoidal curve. The bottom left panel displays the distribution of the stellar velocities with respect to the distance from the best-fit axis of rotation (with position angle PA_0), projected along the direction perpendicular to it (X'). The bottom right panel reports the cumulative velocity distribution of stars with $X'(PA_0) > 0$ and $X'(PA_0) < 0$ (dotted line) and the KS test result.

The KS test is used to determine whether the two samples differ significantly. The resulting probability labelled in the panel determines if the two datasets belong to the same parent population. We obtained $PA_0 = -46$ degrees and an amplitude of $4.9km/s$. This value well agrees with those previously obtained by Bellazzini(2012) and Bianchini et al.(2013) who found $4.40km/s$ and $4.970km/s$, respectively.

The KS test rules out that the two samples are extracted from the same population, confirming the different distribution of the samples with $X'<0$ and $X'>0$.

Bianchini (2013) found a differential rotation for 47Tuc, meaning that different regions of the cluster rotate at different velocity. In particular, they found a rigid rotation behaviour in the central region, and a sharp decline in the outer parts, with the amplitude varying from $A \sim 5km/s$ in the internal part to $A \sim 4km/s$ out to $80r_c$. In order to evaluate the possible differential rotation, we selected three different bins: $(14 - 300)arcsec$, $(300 - 570)arcsec$, $(570 - 800)arcsec$. The result is shown in figures 4.8, 4.9, 4.10. As can be seen the rotation is more evident in the central part of the cluster (with an amplitude of $5.1km/s$) and decreases towards the external regions (down to an amplitude of 4.7 km/s), although the difference is lower than 0.5km/s.

We searched for differential rotation also dividing the sample in finer radial bins. However, the limited number of stars does not allow to get conclusive results as shown in Figure 4.11.
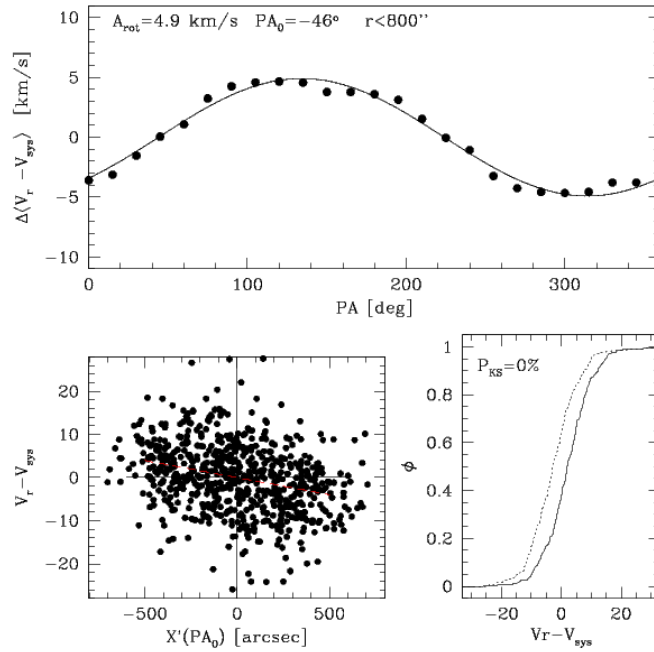
Figure 4.7: The rotation curve obtained by using the entire sample of radial velocities of 47Tuc. The upper panel shows the difference between the mean radial velocities determined in the two halves of the sample, as a function of the position angle PA. Labelled are the best-fit values of the rotation curve amplitude (A) and rotation axis position angle (PA_0). The left bottom panel shows the star velocity distribution as a function of the projected distance (X') from the rotation axis. The right bottom panel reports the results of the KS test and the cumulative velocity distribution of stars.
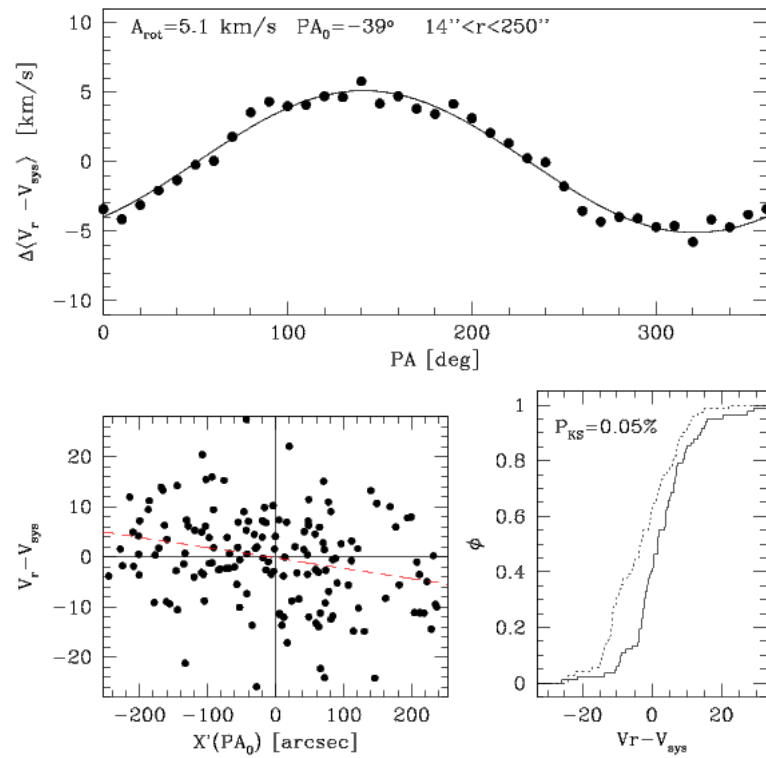
Figure 4.8: Study of the rotation curve of 47 Tucanae in the most internal region (14arcsec<r<250arcsec) sampled by our spectroscopic data set. Each panel has the same meaning as in Fig. 4.7.
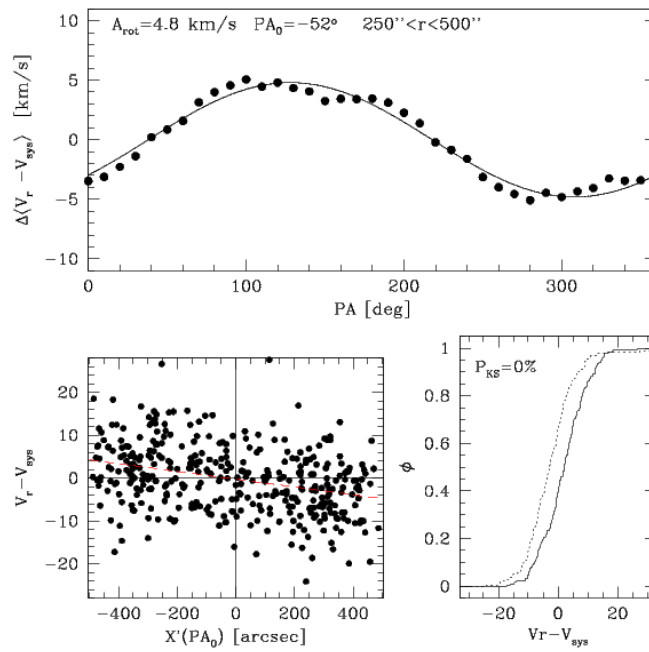
Figure 4.9: Study of the rotation curve of 47 Tucanae in the radial region 250arcsec<r<500arcsec.
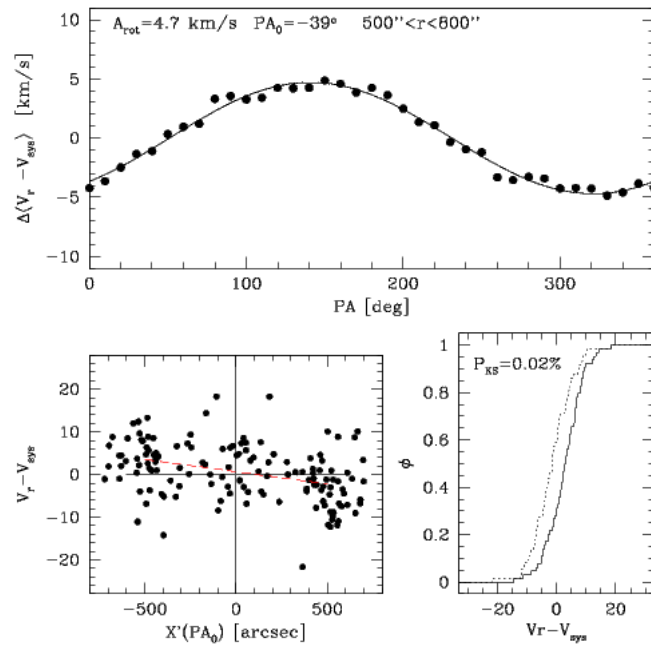
Figure 4.10: Study of the rotation curve of 47 Tucanae in the most external region 500arcsec<r<800arcsec.
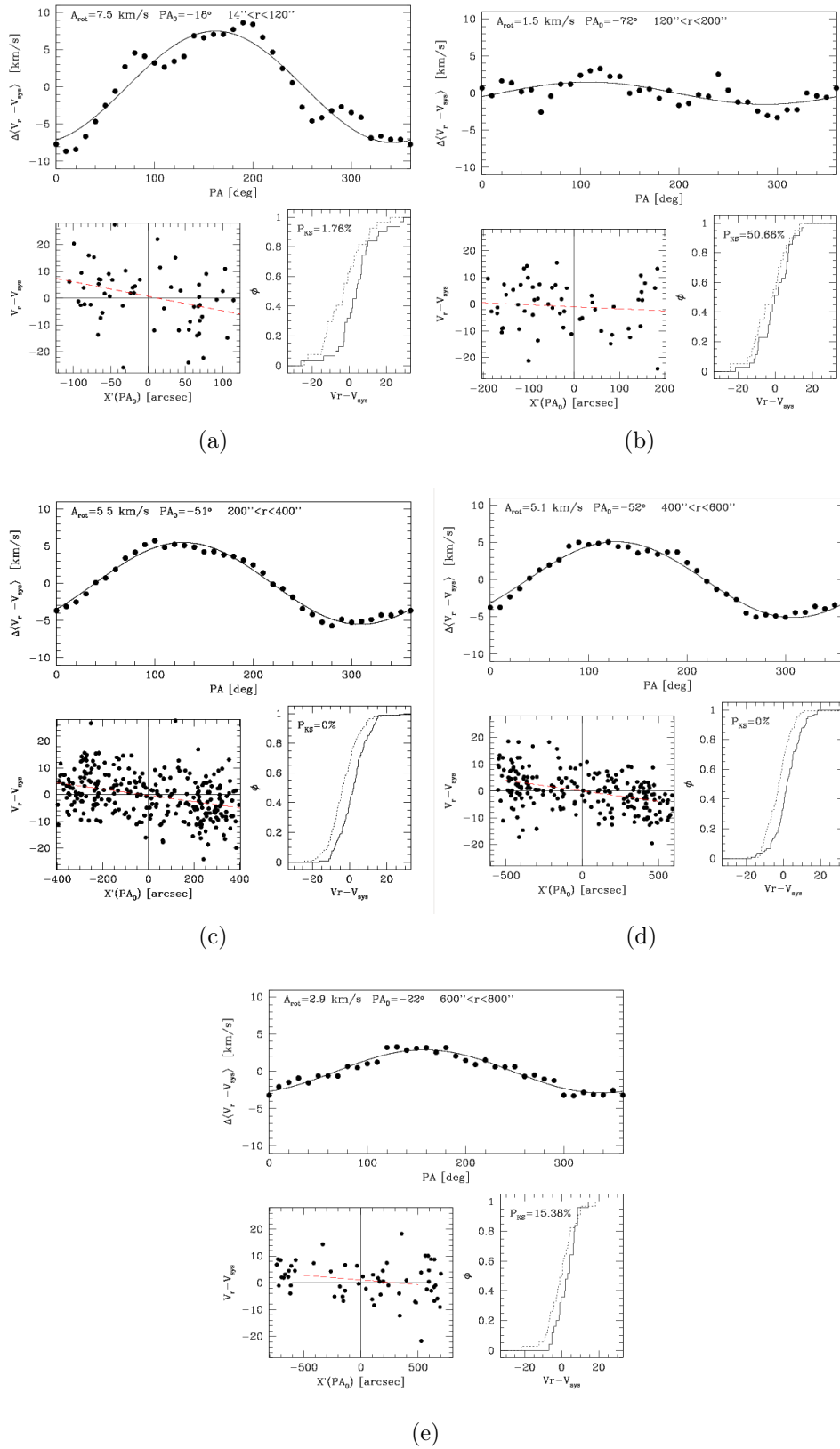
Figure 4.11: Another test of rotation profile, using the velocity dispersion profile selection of bins.

Chapter 5

Summary & Conclusion

By using the high resolution multi-object spectrograph FLAMES/MEDUSA installed at the ESO VLT, we measured the radial velocities of 666 stars of the globular cluster 47Tucanae, between $20 arcsec$ and $79 arcsec$ from the center. The data have been taken from the ESO archive. The entire dataset includes spectra covering different spectral ranges but with similar spectral resolutions, mainly between 16000 and 24000. The analysed stars range from the turnoff region to the tip of the RGB.

The kinematical analysis of this dataset has provided the following results:

1. The mean radial velocity of 47Tuc turns out to be $< v_r >= -17.44 km/s \pm 0.32 km/s$ ($\sigma = 8.26 km/s$). This value well agrees with the previous determinations made by Harris ($< v_r >= -17.40 km/s$) and Lane et al. 2011 ($< v_r >= -16.97 km/s$).

2. The velocity dispersion profile shows a maximum value of $\sigma = 9.80 km/s$ at $< R >= 79 arcsec$ and a subsequent decrease at larger radii, reaching a value of $\sigma = 5.90 km/s$ at $< R >= 665 arcsec$.

   The largest dataset available in the literature for radial velocities in 47 Tuc is that by Lane et al. 2011 who found a behaviour similar to that found in this study but for the innermost region. In fact, the velocity dispersion found at $< R >= 79 arcsec$ is $8.4 km/s$, lower than our one. We conclude that this difference is due to the different rejection criteria of the outliers adopted in the two studies: 2σ adopted by Lane et al. 2011 and 2.5σ in this Thesis. The observed profile can be reproduced with a King model with $r_c = 28 arcsec$ and $\sigma_0 = 11.6 km/s$.

3. We found evidence of rotation along the entire cluster extension, with an average amplitude of $4.9 km/s$. This value nicely matches the previous measures of rotation for 47 Tuc by Bellazzini et al. 2012 and Bianchini et al.

2013. We found evidence of differential rotation, being the rotation lower in the external cluster regions. Also, our derived value of rotation well agrees with the empirical $[Fe/H] - A_{rot}$ found by Bellazzini et al. 2012, indicating that metal-rich GCs have larger rotation with respect metal-poor systems.

5.1 Overall context of the work & Future Perspective

This thesis is part of the Cosmic Lab project, whose goal is to provide the first comprehensive catalog of velocity dispersion and rotational profiles ever obtained for Galactic Globular Clusters, with the final aim of understanding the complex interplay between stellar dynamics and evolution.
To this purpose the radial velocity of hundreds individual stars were measured in 30Gcs, representative of the overall galactic population, with the multi-object spectrographs of the VLT. The observations combine data from FLAMES, for the cluster outskirts, and KMOS, for the central regions, obtained in the context of two ESO Large Programmes.

The future goal of this work is to obtain a final version of velocity dispersion profile in the central bins and the rotation curve along the whole radial sample. These profiles allow us to compare the observed data with appropriate dynamical models and thus to obtain an accurate description of the dynamical status of this cluster. From the comparison with King Models, the shape of the density profile and velocity dispersion profile, in the central part, can be interpreted in terms of the presence or the absence of an IMBH.
The goal of the Cosmic Lab project is to do this kind of study for other clusters, in order to obtain a complete physical description of them and made comparison between their dynamical behaviours.

Bibliography

Alpaslan, M., 2009, *A brief guide to FXCOR*

Archinal, B.A. & Hynes, S.J., Willmann-Bell Inc., 2010, *Star Cluster*

Beccari, G. & Lanzoni, B. et al. 2008, AJ, Volume 679, Number 1

Bellazzini, M. et al. 2015, ApJL, Volume 800, Number 1

Bianchini, P., Varri, A. L., Bertin, G., & Zocchi, A. 2013, ApJ, 772, 67

Carretta, E. & Bragaglia, A. et al. 2009, A&A 505, 117C

D'alessandro, E. & Lanzoni, B., et al. 2008, ApJ, 681, 311

D'orazi, V. & Lucatello, S., et al. 2010, ApJL, 713:L1-L5

Dobrovolskas, V. & Kucinskas, A., et al. 2014, A&A 565, A121

Fregeau, J.M. et al. 2007, IAU Symposium 246

Freire, P.C.C., 2005, ASP Conference Series 328

Gratton, R. , et al. 2010, The Messanger 142

Grindlay, J.E. & Heinke, C., et al. 2001, Science 292,2290

Johnson, C.I., McDonald, I., et al. 2015, AJ, 149, 2, 71

Kacharov, N. & Bianchini, et al. 2014, P., A&A 567, A69

Kucinskas, A. & Dobrovolskas, V., 2014, A&A 568, L4

Lane, R.R. & Kiss, L.L. et al. 2009, MNRAS 400, 917-923

Lane, R.R. & Brewer, B.J., et al. 2010, ApJL, 711:L122-L126

Lane, R.R. & Kiss, L.L. et al. 2010, MNRAS 401, 2521-2530

Lane, R.R. & Kiss, L.L. et al. 2010, MNRAS 406, 2732-2742

Lane, R.R. & Kiss, L.L., et al. 2011, A&A 530, A31

Lane, R.R. & Kupper, A.H.W., et al. 2012, MNRAS 000, 1-2

Lanzafame, A.C., 2015, A&A 576, A80

Lanzoni, B. & Mucciarelli, A. et al. 2013, ApJ 769:107

Lardo, C., et al. 2014, A&A 573, A115

Lutzgendorf, N., et al. 2011, A&A, 533, A36

Maraston, C., 2003, *Stellar population model*

Maraston, C. & Stromback, G., 2011, MNRAS 000, 1-29

Milone, A.P. & Piotto, G., et al. 2011, AJ 744, 58

Mucciarelli, A. & Bellazzini, M.,et al. 2015, ApJ: arxiv:1501.03161

Osterbrock, D.E. & Fulbright, J.P., et al. 1996, PASP 108:277-308

Osterbrock, D.E. & Fulbright, J.P., et al. 1997, PASP 109:614-627

Pizzella A. 2012, *IRAF*

Pooley, D. & Lewin W.H.G., et al. 2003, AJ 591:L131-L134

Richer, H.B., et al. 2013, AJ 771 L15

Sacco, G.C. & Morbidelli, L., et al. 2014, A&A 565, A113

Shen, Z.-X. & Bonifacio, P.,et al. 2010, A&A 524, L2

Simmerer, J., et al. 2013, ApJL, 764:L7

Smiljanic, R. & Korn, A.J., 2014 A&A 570, A122

Thygesen, A.O. & Sbordone, L., et al. 2013, Mem.S.A.It. 75, 282

Thygesen, A.O. & Sbordone, L., et al. 2014, A&A 572, A108

Van de Ven, G., et al. 2006, A&A, 445, 513

Walker, M.G. & Mateo, M. et al. 2006, AJ 131, 2114

VLT Paranal Science Operations GIRAFFE data reduction cookbook (2009)

List of Figures

List of Tables

Acknowledgements